



Evolution of the Koma Bangou Gold Panning Site (Niger) From 1984 to 2020 Using Landsat Imagery

A. Abass Saley, D. Baratoux, L. Baratoux, K. E. Ahoussi, K. A. Yao, K. J. Kouamé

► To cite this version:

A. Abass Saley, D. Baratoux, L. Baratoux, K. E. Ahoussi, K. A. Yao, et al.. Evolution of the Koma Bangou Gold Panning Site (Niger) From 1984 to 2020 Using Landsat Imagery. Earth and Space Science, 2021, 8, 10.1029/2021EA001879 . insu-03661457

HAL Id: insu-03661457

<https://insu.hal.science/insu-03661457>

Submitted on 7 May 2022

HAL is a multi-disciplinary open access archive for the deposit and dissemination of scientific research documents, whether they are published or not. The documents may come from teaching and research institutions in France or abroad, or from public or private research centers.

L'archive ouverte pluridisciplinaire **HAL**, est destinée au dépôt et à la diffusion de documents scientifiques de niveau recherche, publiés ou non, émanant des établissements d'enseignement et de recherche français ou étrangers, des laboratoires publics ou privés.



Distributed under a Creative Commons Attribution - NonCommercial - NoDerivatives 4.0 International License

Earth and Space Science



RESEARCH ARTICLE

10.1029/2021EA001879

Key Points:

- Koma Bangou is the major artisanal gold mining site in Niger and one of the major sites of artisanal gold mining in the Sahel
- Gold panning in Koma Bangou produces waste that degrades and pollutes the environment
- The use of Landsat satellite sensors allows to monitor the evolution of mining activities during four decades (1984–2020)

Supporting Information:

Supporting Information may be found in the online version of this article.

Correspondence to:

A. Abass Saley,
abdoulatif.aa@gmail.com

Citation:

Abass Saley, A., Baratoux, D., Baratoux, L., Ahoussi, K. E., Yao, K. A., & Kouamé, K. J. (2021). Evolution of the Koma Bangou gold panning site (Niger) from 1984 to 2020 using Landsat imagery. *Earth and Space Science*, 8, e2021EA001879. <https://doi.org/10.1029/2021EA001879>



Received 12 JUL 2021

Accepted 5 OCT 2021

Author Contributions:

Conceptualization: A. Abass Saley
Methodology: A. Abass Saley
Supervision: D. Baratoux, L. Baratoux, K. E. Ahoussi, K. A. Yao
Validation: A. Abass Saley, D. Baratoux
Visualization: A. Abass Saley, D. Baratoux, K. E. Ahoussi, K. A. Yao, K. J. Kouamé
Writing – original draft: A. Abass Saley, D. Baratoux, K. E. Ahoussi

Evolution of the Koma Bangou Gold Panning Site (Niger) From 1984 to 2020 Using Landsat Imagery

A. Abass Saley^{1,2} , D. Baratoux^{3,4} , L. Baratoux^{3,4}, K. E. Ahoussi⁴, K. A. Yao², and K. J. Kouamé⁴

¹Ecole des Mines, de l'Industrie et de la Géologie (EMIG), African Center of Excellence in Mining Environment (CEA_EM-EMIG), Niamey, Niger, ²Institut National Polytechnique Houphouët-Boigny, UMRI 68, African Center of Excellence in Mines and Mining Environments (ACE-MEM), Yamoussoukro, Côte d'Ivoire, ³Geosciences Environnement Toulouse, UMR5563, CNRS, Université de Toulouse & IRD, Toulouse, France, ⁴Université Felix Houphouët-Boigny, UFR Sciences de la Terre et des Ressources Minérales (UFR_STRM), Abidjan, Côte d'Ivoire

Abstract The severe drought of 1983–1984 in the Sahel region, and its socio-economic impacts for people relying on farming had for consequence the first major gold rush at Koma Bangou in the southwestern part of Niger. Initiated in 1984, the gold panning activities were interrupted from 1989 to 1999 with exploration permits assigned to the mining industry. The site was reclassified at the year-end 1999 as a gold panning site and artisanal mining resumed until present-day. Gold panning activities such as ore extraction and cyanide processing produced mining waste including rocks, mine tailings, and treatment residues. Mining waste is a serious environmental, health and safety problem. Multispectral Landsat images (TM4-5, ETM7+, OLI/TIRS) acquired between 1984 and 2020 were used to map the spatial evolution of waste generated by gold panning activities at Koma Bangou. Different processing methods were tested, including Minimum Noise Fraction (MNF) transform, Band Ratio (BR), and Feature Oriented Principal Component Selection (FPCS). The FPCS applied to hydroxyl-bearing minerals appears to be most efficient to map gold extraction and cyanidation waste areas. The waste surface associated with ore extraction has increased from 9.43 ha in 1984 to 234.20 ha in 2020, with continuous expansion during the period of clandestine activity (1989–1999). The waste surface associated with cyanidation has increased from 5.56 ha in 2009 (the year of cyanide treatment introduction) to 99.53 ha in 2020. Landsat multispectral imagery proved a suitable data source for monitoring the evolution of gold mining waste and consequences of public policies at Koma Bangou.

Plain Language Summary Artisanal gold mining in Niger is an alternative income-generating activity for farmers. The first gold rush took place in Koma Bangou, in 1984, following the drought of 1983–1984 in order to cope with famine. The gold panning started in 1984, was interrupted during 1989–1999, and then resumed until present day. This work is based on multispectral analysis of almost 40 years of Landsat data to evaluate the evolution of the surface areas associated with gold extraction and cyanidation (cyanidation is a hydrometallurgical technique for extracting gold from ore by converting the gold to a water-soluble coordination complex). Several image processing methods were tested for the purpose of mapping the extension of waste surfaces from 1984 onwards and the area of cyanidation waste from the year of introduction of this technique in 2009. Using the most efficient method, we report that the waste surface associated with gold extraction has increased from 9.43 ha in 1984 to 234.20 ha in 2020 with continuous expansion during the period of clandestine activity (1989–1999). The cyanidation areas have increased from 5.56 ha in 2009 to 99.53 ha in 2020.

1. Introduction

Artisanal and small-scale mining (ASM) is mainly prevalent in developing countries (Abaidoo et al., 2019; S. Keita, 2001; Owusu et al., 2019). A few years ago, small-scale mining was estimated to account for 15%–20% of global non-fuel mineral production (Hentschel et al., 2002). Although the African continent is home to some of the world's most coveted mineral resources, this favorable geological context has largely failed to lead it toward an equitable and sustainable development trajectory (Hilson, 2002). In some African countries, extreme poverty (A. Keita, 2017; Owusu & Dwomoh, 2012) and crop failures due to climate change are driving rural populations, consisting mainly of farmers, to engage in artisanal mining to meet their daily needs. Artisanal mining is currently the most important rural non-farm activity in Africa (Hilson, 2020). It

© 2021 The Authors. Earth and Space Science published by Wiley Periodicals LLC on behalf of American Geophysical Union.
This is an open access article under the terms of the [Creative Commons Attribution-NonCommercial-NoDerivs License](https://creativecommons.org/licenses/by-nc-nd/4.0/), which permits use and distribution in any medium, provided the original work is properly cited, the use is non-commercial and no modifications or adaptations are made.

Writing – review & editing: L. Baratoux

is inextricably linked to economic development and its impact can be important, particularly when it comes to high-value minerals such as gold, silver and gems (Jennings, 1999). In sub-Saharan Africa, artisanal gold mining has grown over the years in several countries and is now a source of income for hundreds of thousands of farmers (Mallo, 2012; Martin & Hélène, 2017). Artisanal and small-scale mining activities have provided employment to over 2 million people in sub-Saharan Africa (Hilson, 2009). It involves a large number of people and generates significant revenues (Garba Hamidou, 2019; Grandin & Traoré, 1991; Grégoire & Gagnol, 2017; Hilson, 2002; Martin & Hélène, 2017; Organisation de Coopération et de Développement Économiques, 2018).

In Niger, the gold panning activities took place following the 1983–1984 drought and subsequent crop failure (Hilson et al., 2019; Pétot, 1995; Razack, 2002; Yonlihinza, 2017). Artisanal and small-scale mining activities, which were essentially illegal and clandestine in Niger, are now governed by the Law No. 2006-026 of August 9, 2006 and the Ordinance No. 2017-03 of June 30, 2017 (Ministère des Mines et de l'énergie, 2006; République du Niger, 2017). For example, under Niger's mining code, the areas where artisanal mining can be authorized are defined by the regulation. The sites selected for artisanal mining are parcelized in rectangular forms whose sides never exceed one kilometer. Artisanal exploitation plots are granted for a renewable period of two years, to artisanal miners's cooperatives, individuals or to groups of economic interests. The artisanal mining permit confers on its holder, within the limits of its perimeter, and up to a depth of 30 m in the case of step mining and 10 m in the case of surface mining, the right to prospect and mine the substances for which it is issued.

Two main goldfields are located in the western part (Tillabéri region, called Liptako) and the northern part (Agadez region) of Niger (Figure 1). More than 69 official gold panning sites are located in the region of Tillabéri (Organisation de Coopération et de Développement Économiques, 2018) (Figures 2b and 2c). In the Agadez region, approximately 60 gold panning sites are located in the Djado mountains, and 14 sites in the Tchibarakaten gold fields (Pellerin, 2017), addition to the Tabélot sites. Some gold panning activities are also present in the southern part of the Maradi region, in the department of Madarounfa, near the Nigerian border.

Artisanal gold mining in Niger is a seasonal income-generating activity (Razack, 2002) and it is the most important source of income in many rural localities (Hilson et al., 2019). These gold mining activities currently involve more than four hundred fifty thousand (450,000) people and more than two million seven hundred thousand (2,700,000) people depend on it, in Niger (Hilson, 2016; Organisation de Coopération et de Développement Économiques, 2018). These activities produce between two and five tons of gold per year in the Tillabéri region (Organisation de Coopération et de Développement Économiques, 2018), and approximately 10 tons of gold were produced per year in the Agadez region (Grégoire & Gagnol, 2017). Overall, the extractive sector including industrial mining in Niger accounts for 83.43% of the Niger total exports, 22.66% of the government revenues, and 10% of the gross domestic product (GDP) (Organisation de Coopération et de Développement Économiques, 2018). In addition to indigenous people, gold panners came essentially from other regions of Niger but also from other African countries such as Algeria, Benin, Burkina Faso, Chad, Ghana, Ivory Cost, Libya, Mali, Nigeria, Sudan, and Togo (Razack, 2002; Yonlihinza, 2017; Organisation de Coopération et de Développement Économiques, 2018).

The first major gold rush at Koma Bangou, in Niger's Liptako, took place in 1984 with the aim of making revenue to better overcome famine and reduce the rural exodus (Organisation Internationale du Travail, 2009). Gold panning activities at the Koma Bangou site were interrupted from 1989 to 1999 due to prospecting by a Canadian company (Etruscan Resources Inc.) and the National Office of Niger Mining Resources (ONAR-EM) (Mobbs, 1997). The site was exclusively dedicated to the gold panning by the Niger government since late 1999. Since this date, the population of gold panners in Koma Bangou has grown considerably as a result of the various gold rushes in the area. The population has grown from two hundred (200) in 1999, when the site was reopened, to twenty five thousand (25,000) in 2001 (Razack, 2002), and to over three hundred thousand (300,000) in 2020, according to the Koma Bangou village chief (asked in April 2020). The Koma Bangou gold panning site is considered as the most active and attractive one in Niger (Hilson et al., 2019).

However, although artisanal and small-scale mining activities contribute to local economies, social and economic development in low-income countries, it has significant environmental, social, safety and health

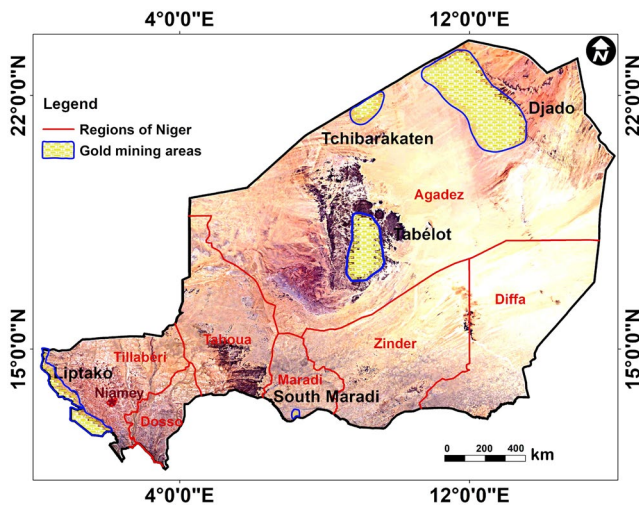


Figure 1. Map of the main gold panning activity areas in Niger overlaid on the Google Earth image of the country.

impacts (Adon Simon et al., 2016; Alibert et al., 2011; Alshaebi et al., 2009; Callil & Junk, 2010; Hilson, 2002; Martin & Hélène, 2017; Mkpuma et al., 2015; Mudd, 2007; Omara et al., 2019; Sheriff et al., 2018). These artisanal gold mining activities contribute to deforestation, land degradation, soil, water, and air pollution, and are responsible for the loss of the biodiversity (Amadou & Bouzou, 2016; Association Vie et Développement, 2018; Organisation Internationale du Travail, 2009; Ousseini Zakaria et al., 2018, 2019; Razack, 2002; Tankari Dan-Badjo et al., 2014, 2019; Yacouba, 2015). In order to obtain the metal of gold, large amounts of land are mined and large quantities of ore are treated with chemicals such as mercury, cyanide, and acids (Garba Hamidou, 2019; Organisation Internationale du Travail, 2009). The extracting and processing of ore at the Koma Bangou site generate waste and destroy vegetation, soil, and fauna and spoil water resources (Association Vie et Développement, 2018).

To better manage the artisanal gold mining activities, it is first necessary to accurately map and monitor the waste extent. The use of remotely sensing techniques, including satellite imagery, has proven useful for this purpose (Barenblitt et al., 2021; Forkuor et al., 2020; Hao et al., 2019; Khalifa & Arnous, 2012; Marcangeli, 2003; Mensah et al., 2017; Ngom et al., 2020; Nodem et al., 2019; Paull et al., 2006; Schimmer, 2008; Sonter et al., 2014;

Suresh & Jain, 2013; Werner et al., 2019, 2020, 2020; Woldai, 2001; Xu et al., 2016). The different Landsat sensors (LS 4–5 TM, LS 7 ETM+, LS 8 OLI/TIR) provide multispectral images that can be effectively used for mapping and monitoring waste. Depending on the geological context, waste contains hydroxyl-bearing minerals, such as clays, and iron minerals, such as iron oxides, that have diagnostic features in the visible and near infrared domain, and may be potentially mapped by using multispectral or hyperspectral data (Plumlee, 1997; Swayze et al., 2000). Multispectral Landsat images covering the Koma Bangou area are used here to track the evolution of the artisanal gold mining site from 1984 to 2020.

The Koma Bangou gold panning area belongs administratively to the region of Tillabéri, in the western part of the Republic of Niger (West Africa). The village of Koma Bangou is located at 14°5'11.00"N and 1°3'48.00"E, in the northern Sahelian climatic zone (Seyni et al., 2014) and the site lies between the Niger River, and its tributary, the Dargol River (Figure 2b). The main economic activities of the population are seasonal agriculture and extensive livestock.

Geologically, the Koma Bangou area is located in the Lower Proterozoic Birimian greenstone belt of Diagorou-Darbani in the western part of Niger, called Liptako, and which forms the northeastern end of the Leo-Man Shield (Figure 2a) (Machens, 1973; Soumaila, 2000). The Birimian basement of Liptako consists of alternating greenstone belts and granitoids oriented NE-SW (Figure 2c) (Dupuis et al., 1991). The host-rocks of the gold mineralization in the Koma Bangou area consist of porphyry quartz diorite and syenite, and meta-volcano-sediments locally subjected to carbonatization and silicification (Poulin et al., 1987). The bed-rock is overlain by lateritic duricrust covered by sandy-clay and eolian alluvium. The gold mineralization at Koma Bangou is of the quartz vein type with native gold, iron, copper and arsenic sulfides paragenesis (Poulin et al., 1987).

2. Materials and Methods

2.1. Data

In order to study the temporal evolution of the Koma Bangou gold panning site over 35 years, scenes from the different Landsat sensors were considered (see Figure S1 in Supporting Information S1). We had focused on Landsat sensors LS 4–5 TM, LS 7 ETM+, LS 8 OLI/TIRS, for which the multispectral bands wavelengths are almost similar (NASA, 2014, 2017) (see Figure S2 in Supporting Information S1 for more details). The wavelengths similarity and relationship between the different multispectral bands from the LS 4–5 TM, LS 7 ETM+ and LS 8 OLI/TIRS sensors provide the opportunity to link different bands from different sensors. The most significant differences are between the Band 5 of Landsat 8, which is much narrower than the

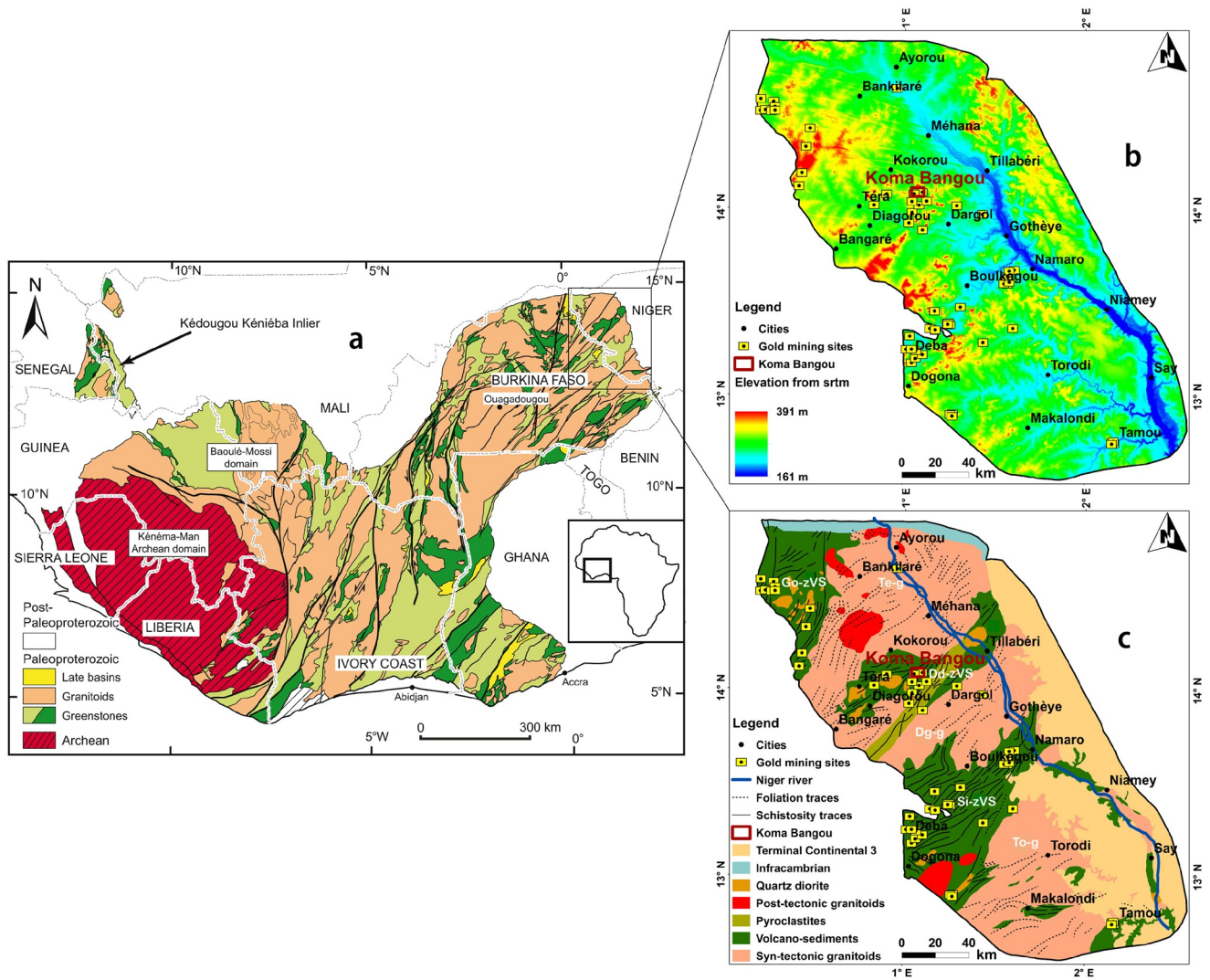


Figure 2. (a) Map of the Leo-Man Shield major geological units (Thiéblemont et al., 2016) modified from Milési et al. (2004); (b) Location of Koma Bangou and the other gold panning sites overlaid on the Shuttle Radar Topography Mission (SRTM) map of the Liptako area (western part of Niger); (c) Major geological units of Liptako Niger (modified after Machens, 1967). Dd-zVS, Diagorou-Darbani greenstone belt; Dg-g, Dargol-Gothèye granitoid; Go-zVS, Gorouol greenstone belt; Si-zVS, Sirba greenstone belt; Te-g, Tera granitoid; To-g, Torodi granitoid.

corresponding Band 4 in Landsat 5 and 7, and the shift toward longer wavelength for Band 7 in Landsat 8 with respect to Band 7 in Landsat 5 and 7. If these bands appear critical in the processing pipeline, particular caution should be paid when extrapolating results between Landsat 8 on one side and Landsat 5 and 7 on the other side. The wavelength domains of Landsat bands are useful to map mining waste, based on mineral characteristics (positions of absorption features). Using past images should be therefore useful to fill the gap of knowledge, since field data are not available for the last decades.

For the current study, thirty-four (34) Landsat cloud-free images of the study area were downloaded from the USGS web site www.earthexplorer.usgs.gov (see Table S1 in Supporting Information S1). The selection process of Landsat images considered in priority the dry period (March–May) when the sky was cloudless and the land surfaces were not covered by seasonal grasses. In the absence of images from this period, available images from the rainy season (June–September) or intermediate season (November to February) were used. A timeline (see Figure S3 in Supporting Information S1) shows the different Landsat images used in this study.

2.2. Waste Mapping Method

This section describes the principle and processing methods for waste mapping, followed by the validation procedure.

2.2.1. Principle

This approach was developed to identify areas of artisanal gold mining activity and to reconstruct the history of gold panning from present time back to the opening of the Koma Bangou gold panning site, from Landsat satellite images and field observations. The method used in this work was based on the use of contrasts between the observed objects and their environment (Gond et al., 2004). In the case of the present study, the observed objects (gold panning areas, including waste from extraction and cyanidation) were distinguished from their environment (lateritic and alluvial cover) based on the contrast between the waste and the surrounding terrain, which was generally a complex response, depending on mineral compositions, and the sensor characteristics, including the spectral bands. In order to amplify this contrast, to isolate the waste properly, Minimum Noise Fraction (MNF), Band Ratio (BR), and Feature Oriented Principal Component Selection (FPCS), based on the knowledge of minerals likely present in waste and their spectral signatures, were applied to each pre-processed Landsat image. The relative performance of each method is then evaluated and the most efficient method was selected for application to the entire time series. Two software packages were used: Envi 5.1 for Landsat images pre-processing, MNF, BR, and FPCS processing, and ArcGIS 10.4 for storage, spatial information extraction, and waste mapping.

2.2.2. Landsat Images Pre-Processing

Several pre-processing operations were applied to the images with Envi 5.1 software including radiometric calibration, atmospheric correction (Envi 5.1 FLAASH module), conversion of radiometric values to reflectance (Han & Nelson, 2014) and the study area image extraction from the pre-processed images. With the failure of the Scan Line Corrector (SLC) on the Landsat 7 Enhanced Thematic Mapper (ETM) sensor on May 31, 2003 (Storey et al., 2005), all images taken from this date onwards show wedge-shaped gaps on both sides of each scene, resulting in a loss of approximately 22% of the data (Storey et al., 2005). To make the images usable, Scaramuzza et al. (2004) developed a technique which can be used to fill gaps in one scene with data from another Landsat scene. A linear transform was applied to the “filling” image to adjust it based on the standard deviation and mean values of each band and of each scene (Mohammdy et al., 2014; Scaramuzza et al., 2004; Storey et al., 2005; Zhou et al., 2020). A pair of Landsat ETM7+ images from the same path and row was used to apply the gap-filling technique to ETM7+ images used in this study, which were found in this condition (see Figure S3 in Supporting Information S1).

2.2.3. Minimum Noise Fraction (MNF)

The MNF is a double pre-processing method applied to the images. The MNF transform consists of a transformation and reduction of noise in images (Berman, 1985; Dabiri & Lang, 2018; Green et al., 1988; Frassy et al., 2013; Shawky et al., 2019). MNF transforms multispectral data that include noisy components into channel images with increasing noise levels, it is therefore a method to separate the noise from the data and reduce computational requirements for further processing (Boardman et al., 1995). MNF is composed of two consecutive principal component (PC) transformations (Green et al., 1988). The first transformation of PC focuses on whitening noise by decorrelating and rescaling the noise in the data, producing data in which the noise has variance one (1) and no correlation from band to band (Shawky et al., 2019). This transformed data is then subjected to a second standard PC transformation, resulting in final outputs that are uncorrelated and are arranged in terms of decreasing information content (Research Systems, Inc., 2003). The MNF transform is widely used for lithological and geological features mapping (Ciampalini et al., 2013; Dadon et al., 2010; Harris et al., 2011; Kumar et al., 2015; Ourhzif et al., 2019; Pournamdari et al., 2014).

2.2.4. Spectral Band Ratio

The BRs have been widely used in the field of mining environment and geological mapping for the purpose of improving the spectral information of specific minerals (Khidir & Babikir, 2013; Kujjo et al., 2018; Masmoumi et al., 2017; Moradi & Boomeri, 2017). In the BR technique, the ratio between two bands is calculated for each pixel. The ratioed image allows better distinction between different lithological units and hydro-thermal alteration zones (Abdelsalam et al., 2000; Abhary & Hassani, 2016; Abrams et al., 1983; Carranza

Table 1
Summary of Used Band Ratios and Feature Oriented Principal Component Selection

Mineral groups	Spectral band name	Wavelength (nm)	TM/ETM + Band ratios and FPCS	OLI8 Band ratios and FPCS
Iron oxides (Hematite, goethite, jarosite)	Red Blue	640–670, 450–510	Ratio 3/1 FPCS Bands 1345	Ratio 4/2 FPCS Bands 2456
Ferrous minerals	(SWIR) 1 (NIR)	1,570–1,650, 850–880	Ratio 5/4	Ratio 6/5
Hydroxyl-bearing minerals such as clays minerals	(SWIR) 1 (SWIR) 2	1,570–1,650 2,110–2,290	Ratio 5/7 FPCS Bands 1457	Ratio 6/7 FPCS Bands 2567

& Hale, 2002; Frutuoso, 2015; Hung, 2013; Mwaniki et al., 2015; Ourhzif et al., 2019; Ramadan et al., 2001; Rigol-Sanchez et al., 2003).

In this study, three BRs were used depending on the mineralogical characteristics of exploited rocks. At first, iron oxides BRs 3/1 and 4/2 for Landsat TM/ETM+ and OLI8, respectively, were applied in order to highlight iron oxides by the presence of bright pixels (Sabins, 1999). The iron oxides BR is useful for detecting ferric iron (Fe^{3+}) oxides such as hematite and goethite (Imbroane et al., 2007; Hung, 2013; Pour et al., 2019; Rockwell, 2013; Soe et al., 2005; Traore et al., 2020). At second, the BRs 5/7 and 6/7 for Landsat TM/ETM+ and OLI8, respectively, were applied in order to highlight hydroxyl-bearing minerals such as clay minerals (kaolinite, montmorillonite and alunite) by the presence of bright pixels (Clark, 1999; Hung, 2013; Imbroane et al., 2007; Sabins, 1999; Soe et al., 2005). Hydroxyl-bearing minerals represent the most common weathering minerals expected to occur in mining waste (Poormirzaee & Oskouei, 2010). The third BRs used, 5/4 and 6/5 for Landsat TM/ETM+ and OLI8, respectively, highlight ferrous minerals as bright pixels (Aliyu & Aliyu, 2020; Carranza & Hale, 2002; Frutuoso, 2015; Ourhzif et al., 2019; \). A color composite ratio image was produced by combining the three ratio (6/7, 6/5, and 4/2) images in red, green and blue (Sabins, 1999) in order to visualize in a single image the areas rich in iron oxides and/or hydroxyl-bearing minerals (Chica-Olmo et al., 2002).

2.2.5. Feature Oriented Principal Component Selection

Principal component analysis (PCA) is a technique that can be used to enhance and separate certain spectral signatures from the background (Gabr et al., 2010). PCA analysis consists of a multivariate statistical technique that selects uncorrelated linear combinations (eigenvector loadings) of variables such that each successively extracted linear combination, or PC has a lower variance (Mia & Fujimitsu, 2012). The number of output PCs is the same as the number of input spectral bands. PC analysis can be used in a standard method by using all available spectral bands or in a selective method by using selected input bands (Van Der Meer et al., 2012). In this work, the FPCS (Crósta & Moore, 1989) was used to highlight iron oxides and hydroxyl-bearing minerals (Aliyu & Aliyu, 2020; Carranza & Hale, 2002; Crósta et al., 2003; Crósta & Moore, 1989; Loughlin, 1991; Soe et al., 2005; Van Der Meer et al., 2012). This FPCS helps to identify and select specific PCs within a data set, in order to enhance certain spectral signatures (Crósta & Moore, 1989; Loughlin, 1991).

To detect the spectral information of iron oxides and hydroxyl-bearing minerals, their spectral signatures obtained from the USGS spectral library (Clark, 1999; Kokaly et al., 2017) were used. Based on this spectral library, the multispectral bands (1, 3, 4, and 5) and (2, 4, 5, and 6) were used for TM-ETM+ and OLI/TIRS, respectively, to highlight the spectral response of iron oxides. The multispectral bands (1, 4, 5, and 7) and (2, 5, 6, and 7) were used for TM-ETM+ and OLI/TIRS, respectively, to enhance hydroxyl-bearing minerals (Osindowo et al., 2021; Pour et al., 2019; Traore et al., 2020). The resulting PCs images could then show targeted surface types such as rocks, waste, soils, villages/settlements by highlighting them as bright or dark pixels, depending on their respective (positive/negative) eigenvector magnitudes and signs (Boateng et al., 2018; Kujjo et al., 2018). For better discrimination and delineation lithology, color composite images were produced by combining three PCs images in red, green and blue channels. Table 1 summarizes the different BRs and FPCS used in this study.

In order to map gold panning waste from previous years, a time series of Landsat images of the study area was used. The Landsat image of the year 2019, for which field data were available, was taken as a reference,

and therefore for validation. The different image processing methods (MNF, BRs, FPCS) were applied to this 2019 Landsat 8 image. Among these methods, the most efficient one to highlight and map the waste was selected. Once the characteristics of the gold panning areas were recognized based on the comparison of image products with the field observations, waste surfaces were extracted from the entire series of Landsat images in vector forms. These vectors constituted the boundaries of the extraction and cyanidation areas of the gold panning site. The vectors were then integrated into a Geographic Information System (GIS) to assess the extent of extraction and cyanidation areas.

2.2.6. Validation and Analysis of the Entire Time Series

The validation of the results was based on the comparison of remote sensing products with the fieldwork observations. The different waste surfaces were mapped and delimited by field GPS coordinates. These GPS coordinates were then integrated into ArcGIS and the waste contours polygons were drawn from these coordinates, and the waste surfaces re-calculated. The results obtained from the Landsat images processing were compared with the results obtained from the GPS field surveys for the year 2019 and a confusion matrix was produced. The validation obtained from 2019 justifies the application of the same method to the entire time series to map extraction and cyanidation areas from 1984 to 2020.

3. Results

3.1. Field Observations and Mapping of Extraction and Cyanidation Areas

3.1.1. Source of the Koma Bangou Gold Panning Waste

The Koma Bangou gold panning waste came from ore extraction pits and treatment (Figure 3). During ore extraction, overburden rocks and rocks hosting the gold-bearing quartz veins were extracted from the pits (Figure 3a). These rocks constituted solid waste which was exposed around the extraction pits and often in the vicinity of habitation. This waste, which was accumulated in heaps, consisted mainly of lateritic and clayey altered rocks, saprolites (Figure 3b) and unaltered rocks such as quartz diorite (Figures 3c and 3d). The quartz veins extracted from the pits were crushed manually (Figure 3e). Before the introduction of the cyanidation treatment technique (2009), the crushed ore was placed in water on a sloping table ("sluice") to recover the gold nuggets (gravimetric method) (Figure 3g). The tailings were mostly stored in the village and were often used to make mud bricks for the houses construction. However, since 2009, with the introduction of the cyanidation technique, some of these tailings were reground (Figure 3h) and transported to the cyanidation areas where they were chemically attacked by a sodium cyanide solution in ponds dug into the ground and sealed with plastic sheeting to recover the remaining gold content (Figure 3i). The gold contained in waste was dissolved and collected on zinc plates through a cementation process. The zinc plates were then treated with nitric and sulfuric acids (Figures 3j and 3k) to recover the gold metal (Figure 3l). This chemical treatment generated solid waste (Figure 3m) and liquid residues (Figures 3n–3p). The solid waste was the residue extracted from the ponds after the ore had been in the cyanide solution for 12–48 hr. These piles of solid waste were often several meters high with large spatial extensions. Liquid residues were the result of the chemical treatment of gold with sulfuric and nitric acids, cyanide residues, zinc solutions, process water, and detergents.

3.1.2. Gold Extraction and Cyanidation Areas Waste Field-Mapping

The waste from the cyanidation process (Figure 4a) and from the ore extraction pits (Figure 4b) was mapped from April 06 to 12, 2019 using a field Global Positioning System (GPS) with ± 3 m resolution. The coordinates of the edges of the waste areas were recorded. These coordinates were then transferred to ArcGIS 10.4. The polygons of the different areas were plotted from these coordinates and their surfaces were calculated in hectares (ha). Figure 4c shows the spatial distribution of extraction and cyanidation areas from the Koma Bangou gold panning site in the year 2019.

3.2. Results of Landsat Image Processing for Waste Mapping

The reference scene used for application of the waste mapping methods was the Landsat 8 OLI/TIRS image acquired on March 04, 2019. The time difference between the image acquisition date and the field survey



Figure 3. The Koma Bangou gold panning waste production: (a) workers operating a hoist on a gold mining pit; (b) clay minerals-rich tailings around dwellings; (c) quartz diorite tailings near houses; (d) ore extraction pit with crushing machines just behind; (e) manual crushing of gold-bearing quartz; (f) quartz ore fragments crushing machine; (g) gravimetric concentration of gold by sluice; (h) grinding machine for the fine residues from the gravimetric concentration; (i) alignment of cyanidation ponds; solution of gold-bearing zinc with nitric acid (j) and sulfuric acid (k); (l) gold concentration by firing with nitric acid and sulfuric acid; (m) pile of cyanidation solid waste; (n) place of acid treatment of gold; (o) acidic liquid residue from the chemical treatment of gold; (p) storage hole for acidic liquid waste.

date (April 06–12, 2019) was not very significant. The methodology applied to this 2019 Landsat 8 image was then applied to all of the collected images (see Table S1 in Supporting Information S1 for all used Landsat images product identifier) with the same image display setting in ArcGIS (Standard Deviations Stretch).

3.2.1. Results of the Minimum Noise Fraction (MNF)

The eigenvalues and percentage eigenvalues (Table 2) of the MNF bands decrease from the first MNF Band to the sixth MNF Bands. According to the eigenvalues, the spectral information is concentrated in the first three bands (Figures 5a–5c). The MNF Band 1 concentrates the maximum information (28.15%), followed by the MNF Band 2 (27.31%) and the MNF Band 3 (17.53%). The other MNF bands (MNF Band 4, MNF Band 5, and MNF Band 6) are poor in spectral information (Figures 5d–5f), with 14%, 9.35% and 2.70% of the eigenvalues respectively for MNF Band 4, MNF Band 5, and MNF Band 6. The MNF Band 1 highlights the major features of the site (extraction, cyanidation and habitation areas) (Figure 5a). The extraction and cyanidation areas are represented in the MNF Band 1 image by bright pixels and the habitation areas by light gray pixels. The MNF Band 2 highlights mainly the cyanidation areas (bright pixels) and the habitation areas (light gray pixels); some extraction areas are also represented by bright pixels (Figure 5b). The MNF

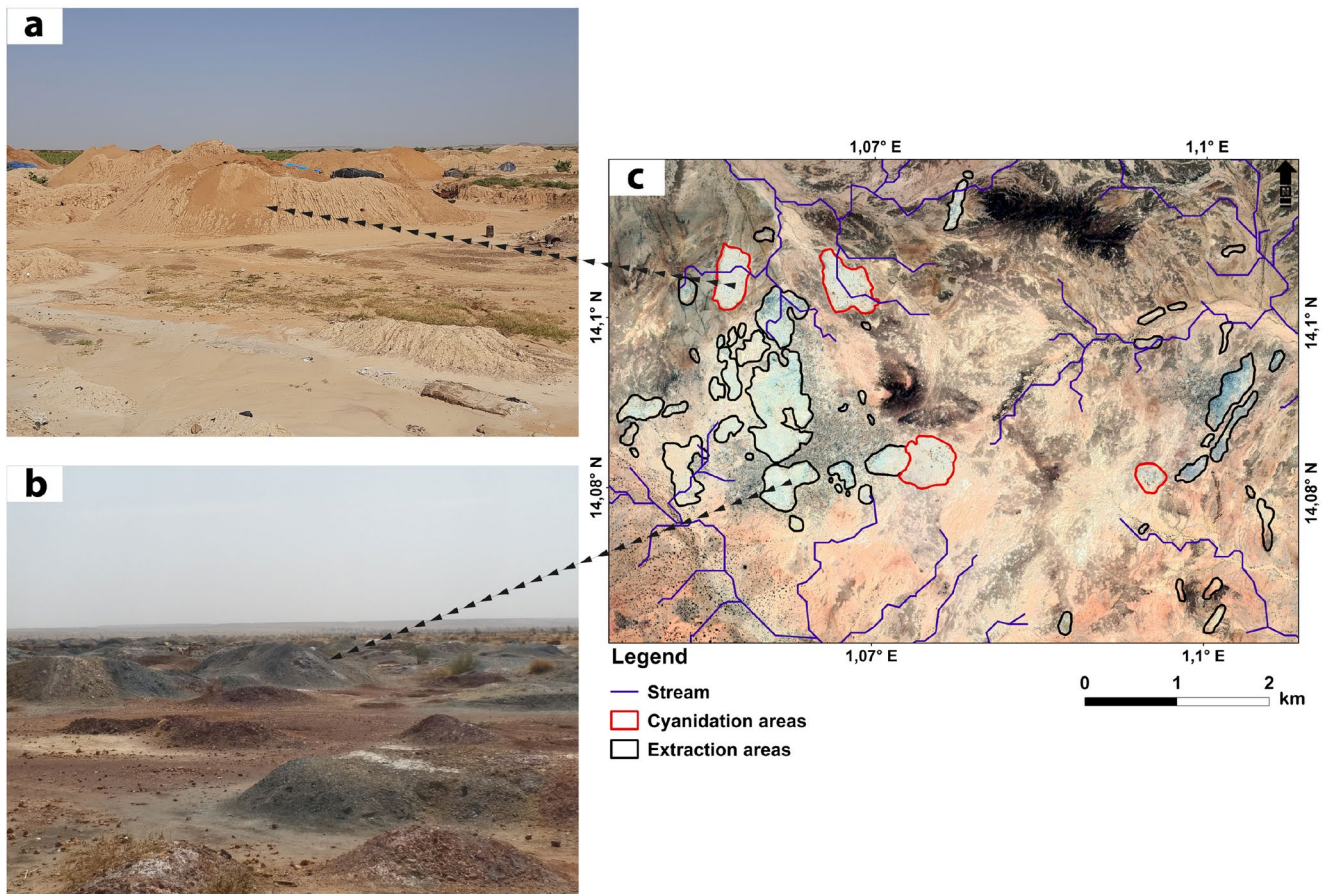


Figure 4. Mapping of the Koma Bangou gold panning waste based on field observations: (a) the cyanidation process waste storage area; (b) waste from ore extraction storage area; (c) map showing hydrographic network of Koma Bangou overlaid on waste surface mapped with GPS data.

Band 3 highlights extraction areas (bright pixels) and the habitation areas (dark pixels); some locations of the cyanidation areas are also represented by dark pixels (Figure 5c). In the MNF Band 5 image, the extraction areas are represented by pixels with varying degrees of brightness, often blending in with habitation (Figure 5e). MNF Band 4 (Figure 5d) and MNF Band 6 (Figure 5f) images do not provide good information to highlight waste or habitation.

The RGB combination of the three bands, MNF Band 1, MNF Band 2, and MNF Band 3, respectively, allows for a better contrast between the extraction waste, cyanidation waste and habitation areas, and better distinction from the bare soils (Figure 6a). Extraction waste is represented by pinkish pixels in the western part and by bright yellow pixels in the eastern part; cyanidation waste is represented by bright yellow pixels, and the habitation areas are represented by deep yellow pixels (Figure 6a). Yellowish areas surrounding the extraction areas could represent a difficulty to precisely delineate the outlines of extraction waste, and there is some possibility of local confusion between extraction areas and other types of land-uses. The RGB color composite of MNF Band 4, MNF Band 5, and MNF Band 6 (Figure 6b) is not useful for highlighting waste. In this representation, there is a strong resemblance between extraction waste and vegetation (green pixels) and between cyanidation waste and other land-uses (brown pixels).

The MNF transformation appears to be useful to delineate the extraction and cyanidation waste with some limitations. The extraction waste is colored in pink and yellow depending on the type of exploited rocks.

Table 2
MNF Bands Eigenvalues and Eigenvalues Percentage

MNF bands	Eigenvalue	Eigenvalue (%)
MNF Band 1	21.89	28.15
MNF Band 2	21.24	27.31
MNF Band 3	13.63	17.53
MNF Band 4	11.64	14.97
MNF Band 5	7.27	9.35
MNF Band 6	2.10	2.70

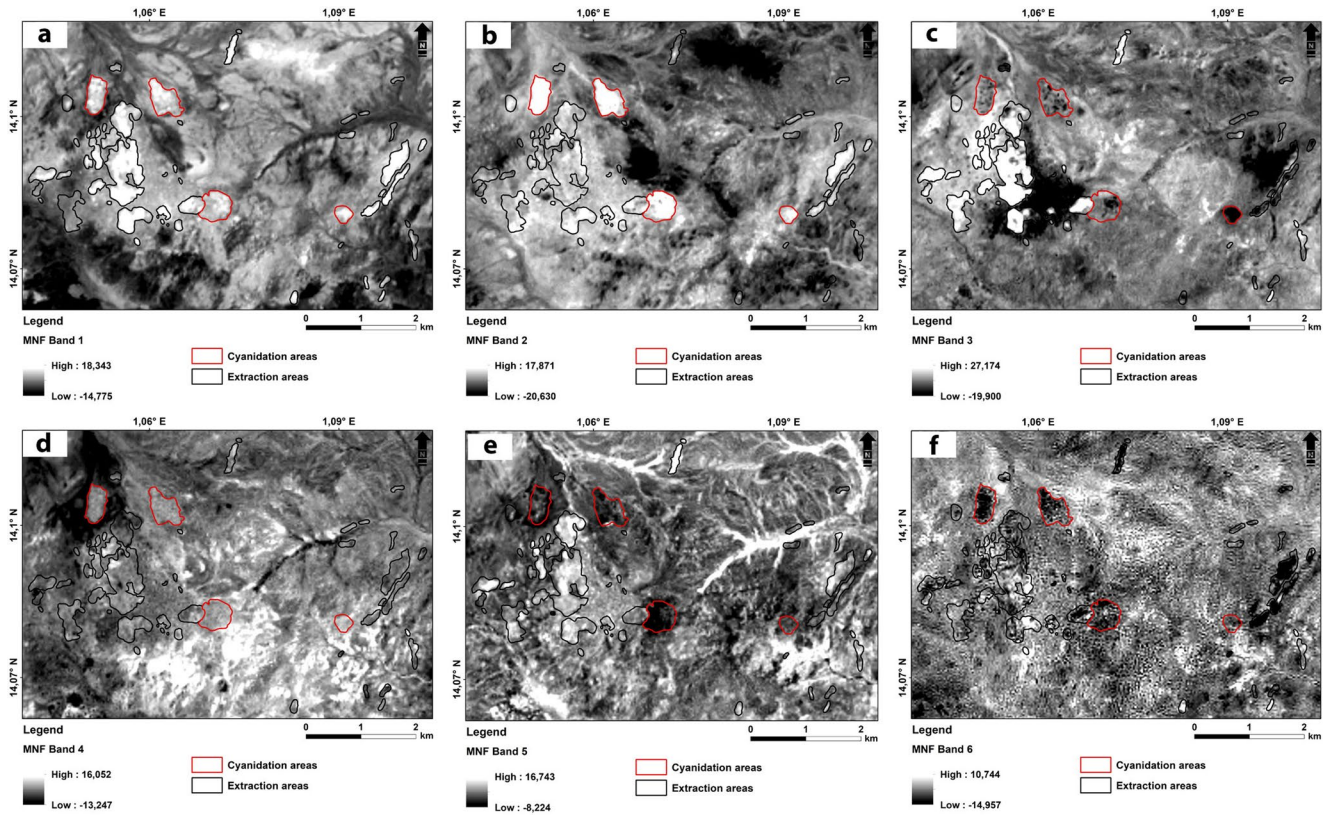


Figure 5. Landsat 8 OLI/TIRS 2019 Minimum Noise Fraction (MNF) bands ((a) MNF Band 1; (b) MNF Band 2; (c) MNF Band 3; (d) MNF Band 4; (e) MNF Band 5; (f) MNF Band 6).

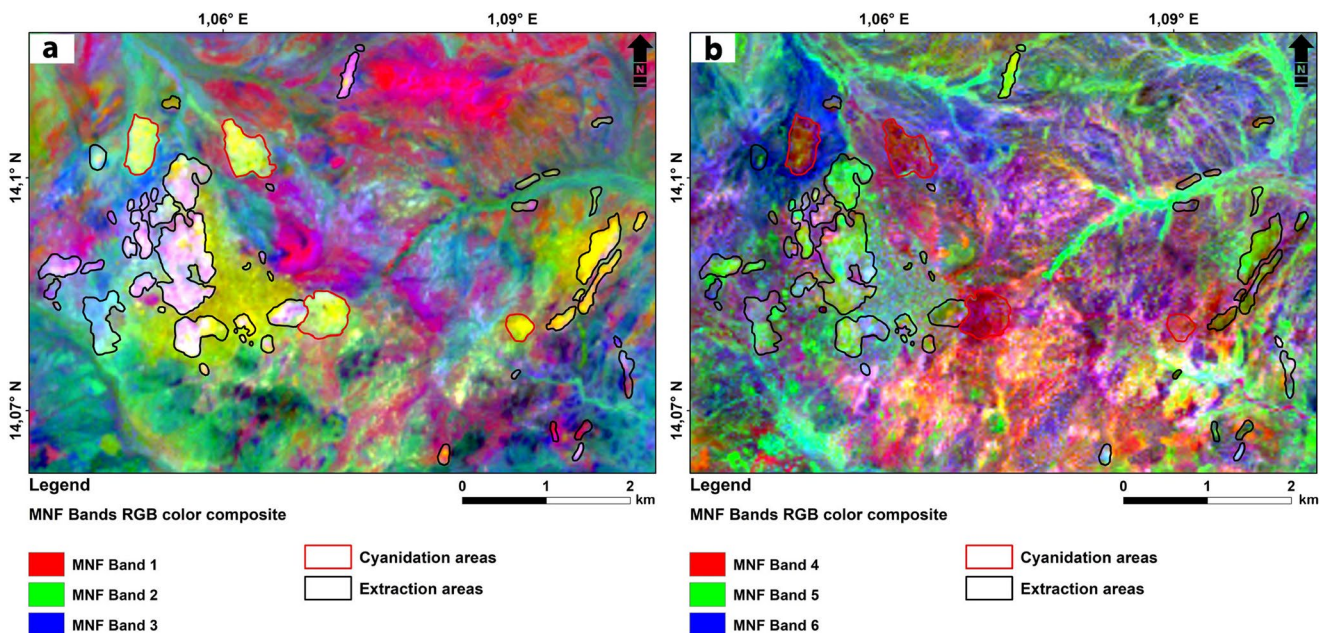


Figure 6. Minimum Noise Fraction (MNF) RGB bands combination: (a) RGB MNF Band 1-Band 2-Band 3; (b) RGB MNF Band 4-Band 5-Band 6.

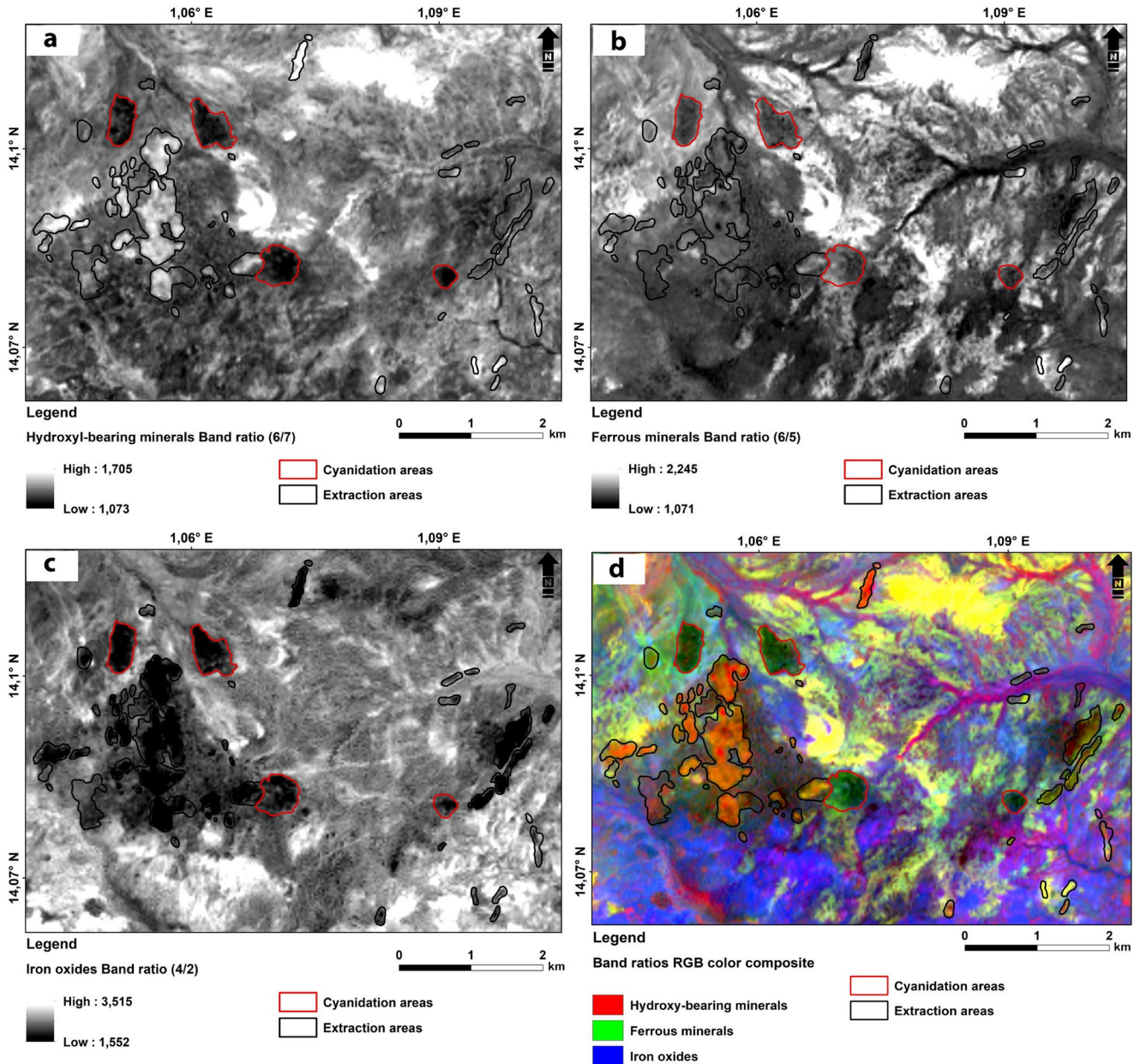


Figure 7. Band ratio results: (a) hydroxyl-bearing minerals, (b) ferrous minerals, (c) iron oxides. The last panel (d) displays the RGB combination of hydroxyl-bearing minerals (R), ferrous minerals (G), and iron oxides (B).

However, the cyanidation waste is not clearly distinguishable from the habitation areas and the yellow-colored extraction areas waste. Therefore, the method of BRs is attempted in the next section to evaluate if it compares advantageously with the MNF method.

3.2.2. Results of Band Ratios

The results of BRs for hydroxyl-bearing minerals, ferrous minerals, and iron oxides are given in Figure 7. Hydroxyl-bearing minerals which have low reflectance (high absorption) at 2.11–2.29 μm and high reflectance at 1.57–1.65 μm , are highlighted by Landsat 8 BR 6/7. The BR image of hydroxyl-bearing minerals highlights the extraction areas represented by bright to light gray pixels and the cyanidation areas represented by dark pixels (Figure 7a). The habitation areas, represented by gray pixels, are not distinguishable in the image. On the Koma Bangou gold panning site, the waste from extraction areas is rich in clay minerals.

Table 3
Results of the Feature Oriented Principal Component Selection for Iron Oxides (a) and Hydroxyl-Bearing Minerals (b)

a: FPCS eigenvalues for iron oxides

Bands	PC1	PC2	PC3	PC4
Band 2	0.166	−0.458	−0.506	0.711
Band 4	0.508	−0.375	−0.414	−0.656
Band 5	0.679	−0.188	0.680	0.204
Band 6	0.504	0.783	−0.331	0.151
%Eigenvalue	89.20	6.73	3.36	0.72

b: FPCS eigenvalues for hydroxyl-bearing minerals

Bands	PC1	PC2	PC3	PC4
Band 2	0.142	−0.418	0.897	−0.003
Band 5	0.648	−0.630	−0.397	−0.158
Band 6	0.507	0.565	0.180	−0.626
Band 7	0.550	0.331	0.069	0.764
%Eigenvalue	89.86	6.27	2.38	1.49

This BR highlights the extraction waste containing clay minerals by bright pixels. On the other hand, the cyanidation waste, which is very poor in hydroxyl-bearing minerals, is highlighted by dark pixels. The BR image of the ferrous minerals (Figure 7b) does not highlight waste with characteristic-colored pixels. Waste and habitation areas are colored in gray without contrast. It is hard to separate waste and habitation from sandy surfaces of bare soils also colored in gray. Iron oxides which have a low reflectance at 0.45–0.51 μm and high reflectance at 0.64–0.67 μm , are highlighted by Landsat 8 BR 4/2. The resulting iron oxides BR image highlights the extraction and cyanidation areas represented by dark pixels (Figure 7c). The habitation areas are represented by gray pixels. The bright pixels are associated with lateritic duricrust. The waste from the Koma Bangou gold panning area is poor in iron oxides and is represented by dark pixels.

The RGB combination (Chica-Olmo et al., 2002) of Landsat 8 OLI/TIRS BRs 6/7, 6/5, and 4/2, respectively (Figure 7d), is efficient in mapping the different rock units in the study area. The waste from extraction areas containing clay minerals appears orange to reddish at the western part and light green at the eastern part of the gold panning area, while the waste from cyanidation areas appears in dark green. This might reflect the relative absence of ferrous iron in this cyanidation waste. The habitation areas appear in brown and dark, whereas lateritic bare soils appear in yellow and sandy bare soils in blue. Vegetation and certain rocky surfaces appear in magenta.

The BR method proves to be effective in mapping the Koma Bangou gold panning waste and other features. The method is efficient at highlighting and discriminating between extraction waste, cyanidation waste, habitation areas and other land-uses areas. Its performance is better than the MNF transform. As the BR method directly used the spectral bands information of certain minerals to discriminate them, it would be useful to also explore the FPCS method, which also used the spectral characteristics of certain minerals such as iron oxides and hydroxyl-bearing minerals associated with mining waste.

3.2.3. Results of the Feature Oriented Principal Component Selection (FPCS)

To map preferentially iron oxides and hydroxyl-bearing minerals contained in the gold panning waste, two applications of the FPCS method are considered here, one for the iron oxides, and the other for the hydroxyl-bearing minerals (Table 3).

The results of the FPCS for iron oxides applied on bands 2, 4, 5, and 6 of the Landsat 8 OLI/TIRS 2019 scene are given in Table 3a. The PC1 concentrates 89.20% of the spectral data variance and represents the combined signature of topography and surface albedo. This PC1 image does not highlight gold panning waste or habitation (Figure 8a). The PC2 concentrates 6.73% of the spectral data variance and its vector

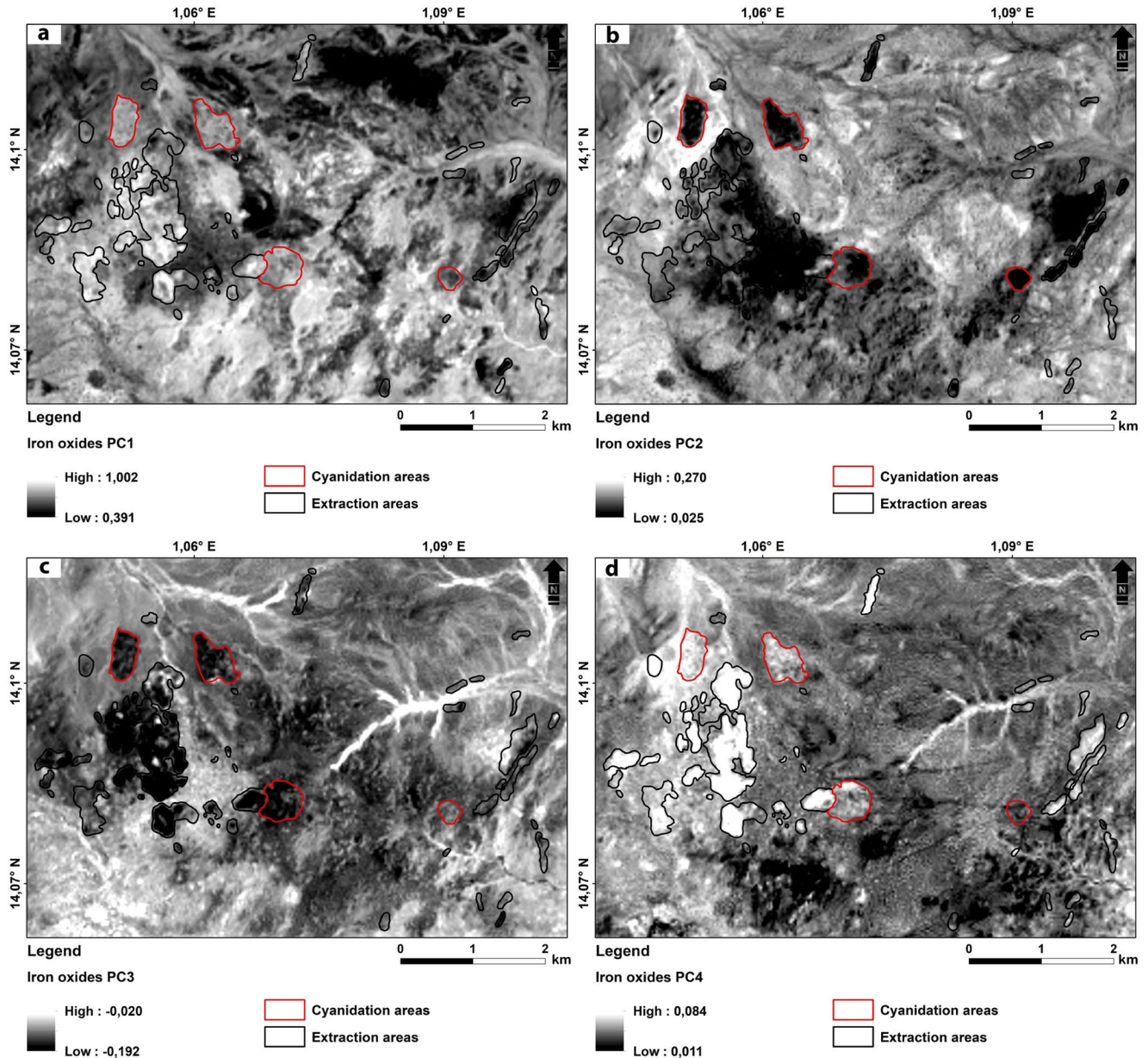


Figure 8. Feature Oriented Principal Component Selection results for iron oxides ((a) PC1; (b) PC2; (c) PC3; (d) PC4).

image highlights the extraction and cyanidation waste, and the habitation areas in dark pixels (Figure 8b). The PC3 concentrates 3.36% of the spectral data variance and its vector image highlights extraction and cyanidation areas as dark pixels; habitation areas are represented by light gray to bright pixels (Figure 8c). The PC4 concentrates 0.72% of the spectral data variance and its coordinates show a strong weight of Band 2 (0.711) and Band 4 (−0.656). This component exhibits the absorption and reflectance characteristics of iron oxides highlighted by the ratio 4/2 of Landsat 8. According to the negative sign of the eigenvalues, the PC4 vector image (Figure 8d), in this condition, highlights iron oxides surfaces as bright pixels. The extraction and cyanidation waste are highlighted as bright pixels, whereas habitation areas appear as light gray pixels.

The results of the FPCS for hydroxyl-bearing minerals applied on the bands 2, 5, 6, and 7 of the Landsat 8 OLI/TIRS 2019 scene are given in Table 3b. The PC1 concentrates 89.86% of the spectral data variance and represents the signature of topography and surface albedo. The PC1 image does not highlight waste or habitation (Figure 9a). The PC2 concentrates 6.27% of the spectral data variance and its vector image presents

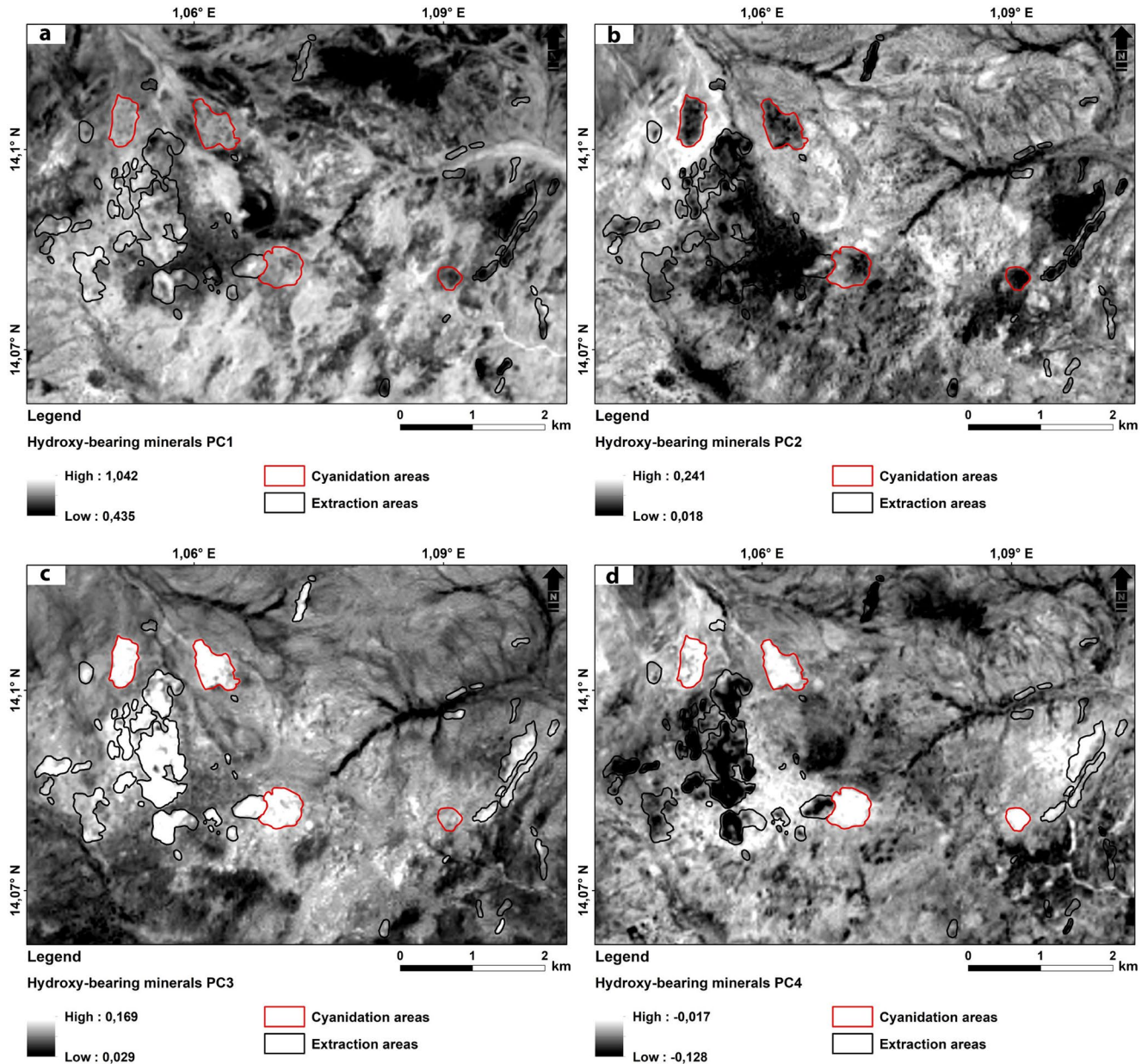


Figure 9. Feature Oriented Principal Component Selection results for hydroxyl-bearing minerals ((a) PC1; (b) PC2; (c) PC3; (d) PC4).

waste from the extraction areas as gray pixels, while cyanidation waste and habitation areas appear as dark pixels (Figure 9b). The PC3 concentrates 2.38% of the spectral data variance and the resulting PC3 vector image highlights the extraction and cyanidation areas as bright pixels and habitation in gray pixels (Figure 9c). The PC4 concentrates 1.49% of the spectral data variance and its coordinates show a strong weight of Band 6 (−0.626) and Band 7 (0.764). This component exhibits the absorption and reflectance characteristics of hydroxyl-bearing minerals highlighted by the ratio 6/7 of Landsat 8. According to the negative sign of the eigenvalues for Band 6 and Band 7, the PC4 vector image (Figure 9d), in this condition, highlights the hydroxyl-bearing minerals as dark pixels. The extraction waste is highlighted as dark pixels, whereas the cyanidation waste and habitation areas appear as bright pixels.

For a better identification and discrimination of waste and habitation from the other land-uses, the three last PCs bands from iron oxides and hydroxyl-bearing minerals FPCS are combined to form a color composite into Red-Green-Blue mode (Figure 10). For the iron oxides FPCS, the RGB color combination of the

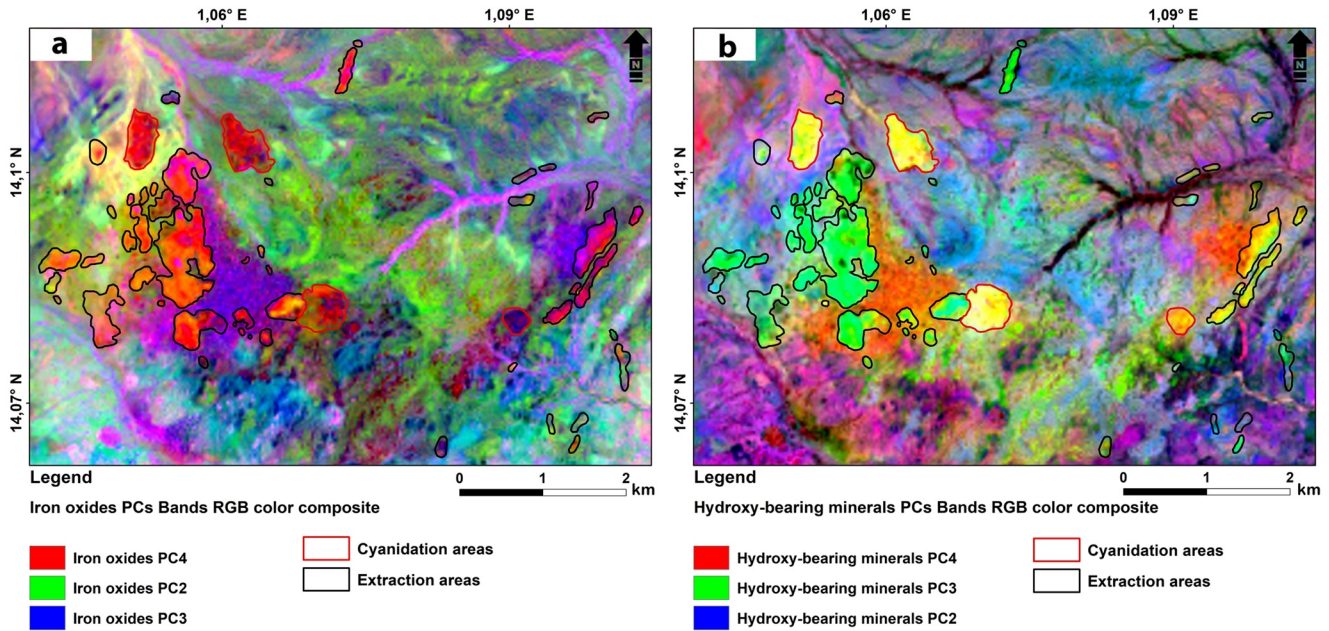


Figure 10. Feature Oriented Principal Component Selection results for iron oxides and hydroxyl-bearing minerals using RGB combination: (a) iron oxides ($R = PC4$, $G = PC2$, $B = PC3$); (b) hydroxyl-bearing minerals ($R = PC4$, $G = PC3$, $B = PC2$).

PC4, PC2, and PC3 bands (Figure 10a), allows for a better contrast between waste and habitation areas. It distinguishes waste and habitation from the bare soils. Extraction and cyanidation waste is represented by orange to red pixels and habitation areas, by blue to magenta pixels. However, this RGB combination is not efficient at discriminating between extraction and cyanidation waste in a red shade. For the hydroxyl-bearing minerals FPCS, the RGB color composite of the PC4, PC3, and PC2 bands (Figure 10b), allows for a better discrimination between extraction waste, cyanidation waste and habitation areas. This color composite also distinguishes waste and habitation from the other land-uses. The extraction waste is represented by green and slightly yellow pixels; the cyanidation waste is represented by yellow pixels and habitation areas by orange pixels.

After the color composite of FPCS for iron oxides and hydroxyl-bearing minerals PCs bands, another FPCS color composite was created. This standard FPCS is commonly found in the literature (Loughlin, 1991). According to the eigenvalues of iron oxides and hydroxyl-bearing minerals PCs bands (Table 3), the PC4 image for iron oxides and the PC4 image for hydroxyl-bearing minerals were negated (all pixel values were multiplied by -1) in order to have BRs of 4/2 for iron oxides and 6/7 for hydroxyl-bearing minerals. This transformation displays iron oxides and hydroxyl-bearing minerals as bright pixels. The new hydroxyl-bearing minerals image provided in bright pixels is called Hydrox Band (Figure 11a), and the new iron oxides image provided in bright pixels is called FeOx Band (Figure 11b). In the Hydrox band image, the extraction waste is highlighted as bright pixels, the cyanidation waste and the habitation areas are represented with dark pixels. The FeOx band image highlights extraction and cyanidation waste as dark pixels. The information in the two new bands is summed up to produce a new image (FeOx + Hydrox Band) displaying the pixels with anomalous concentrations of both iron oxides and hydroxyl-bearing minerals as the brightest (Figure 11c). In this new image, the extraction waste is represented by light gray pixels, the cyanidation waste and the habitation areas are represented by dark pixels. A color composite image of the Hydrox in red, (FeOx + Hydrox) in green and FeOx in blue was created to display the superficial hydroxyl-bearing minerals and iron oxides contained in the waste. This standard FPCS color composite highlights the extraction waste in yellow at the eastern part, and in brown at the western part; the cyanidation waste and habitation appear in blue (Figure 11d).

Comparing the three FPCS applied to iron oxides and hydroxyl-bearing minerals (Figure 12), the FPCS color composite for hydroxyl-bearing minerals (Figure 12b) better identifies and discriminates the gold panning

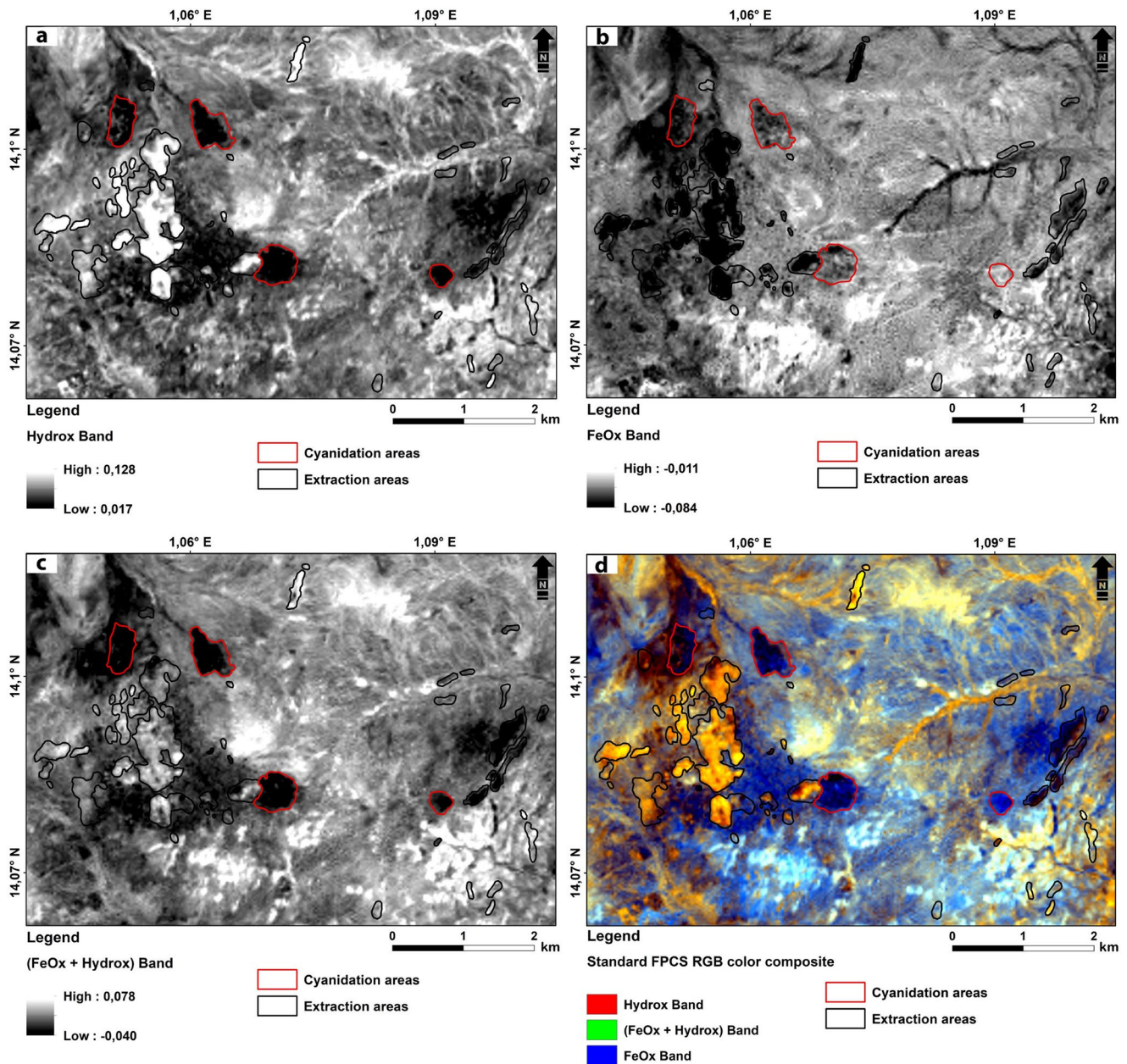


Figure 11. Standard Feature Oriented Principal Component Selection results ((a) Hydrox; (b) FeOx; (c) FeOx + Hydrox; (d) RGB FeOx – (FeOx + Hydrox) – Hydrox).

waste and the habitation areas than the FPCS color composite for iron oxides (Figure 12a) and the Standard FPCS color composite for iron oxides and hydroxyl-bearing minerals (Figure 12c). Therefore, for the PCA, the FPCS method applied to hydroxyl-bearing minerals, which gives the best result on mapping waste and habitation, is selected and retained for the next step (selection and validation of the most efficient method).

4. Choice and Validation of the Method for Application to the Time Series

The approaches used to map the mining area from Landsat images have shown different performances. The color composite bands from the MNF transform (Figure 13a) and the BRs (Figure 13b) methods are less efficient than the FPCS method applied to hydroxyl-bearing minerals (Figure 13c). So, the FPCS method applied to hydroxyl-bearing minerals (Figure 13c) appears to be the most efficient and effective for mapping

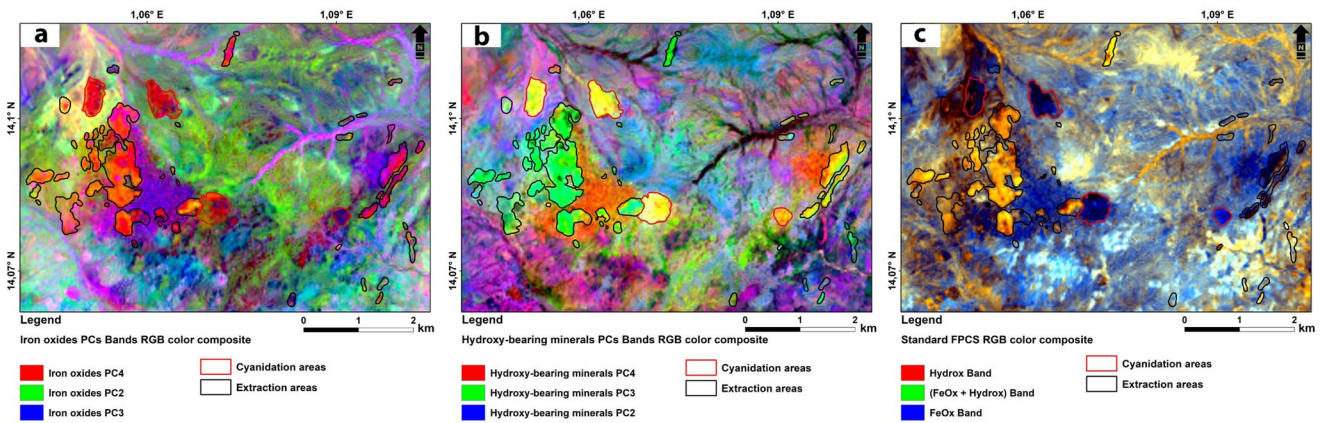


Figure 12. Feature Oriented Principal Component Selection (FPCS) color composite results: (a) for iron oxides ($R = PC4$, $G = PC2$, $B = PC3$); (b) for hydroxyl-bearing minerals ($R = PC4$, $G = PC3$, $B = PC2$); (c) Standard FPCS color composite ($R = \text{Hydrox}$, $G = \text{FeOx} + \text{Hydrox}$, $B = \text{FeOx}$).

waste, habitation and other land-uses. The extraction of waste contours is done manually by using polygons to delineate the waste areas that appear on the processed Landsat images. After overlaying the field surveys with the obtained results (Figure 13), the best match with the field data is obtained with the FPCS for hydroxyl-bearing minerals (Figure 13c). Its high performance is due to the strong presence of clay minerals within the weathering profile of the rocks that were mined at the Koma Bangou site. Indeed, these rocks, composed essentially of meta-volcanites, meta-sediments, and quartz diorite and syenite had undergone meteoric and hydrothermal alteration resulting in the formation of clay minerals, easily identified with the FPCS bands sensitive to hydroxyl-bearing minerals.

In order to further validate this choice for the application to the entire Landsat time series, the confusion matrix between the areas extracted from GPS and those extracted from Landsat image processing is calculated. Table 4 shows that a fraction of extraction and cyanidation areas are misclassified as other areas (19.94% and 27.74%, respectively), meaning that the extent of gold panning areas and impact on the environment could be slightly underevaluated. The examination of the locations of these misclassified areas indicates that they are generally located at the border of the mining areas. Therefore, the approach does not miss mining sites, but it is not perfectly accurate in delineating the borders of the extraction or cyanidation areas. The rate of classification of other land-uses areas as extraction and cyanidation waste is less than 1% (<0.1%). This proves that there is no misclassification of other land-uses areas into mining-affected areas.

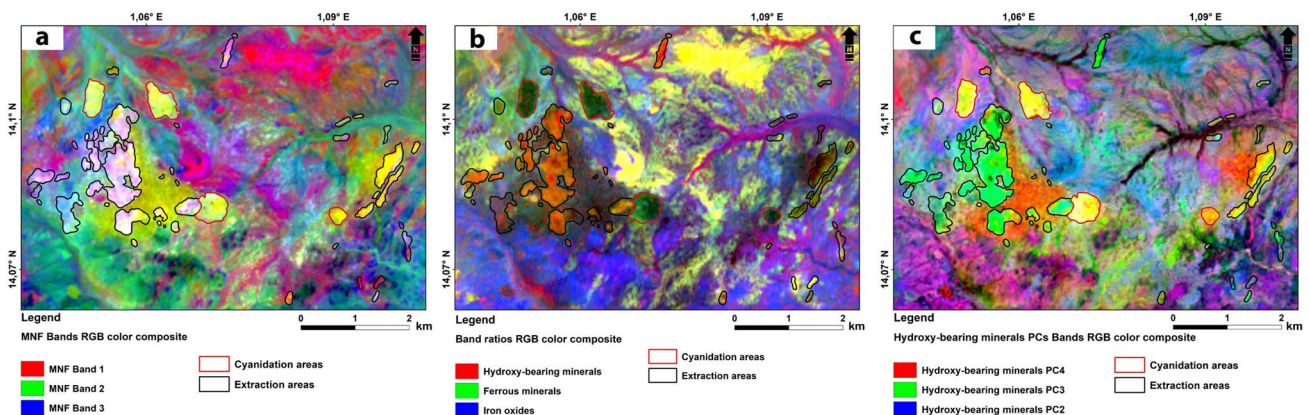


Figure 13. Results of different methods used to map waste areas from the Koma Bangou gold panning area: (a) result of Minimum Noise Fraction (MNF) transform; (b) result of band ratios combination; (c) result of Feature Oriented Principal Component Selection method designed to identify hydroxyl-bearing minerals.

Table 4
Confusion Matrix Between GPS Areas and Landsat Processing Areas

GPS	Landsat		
	Extraction areas	Cyanidation areas	Other types of land-uses
Extraction areas	79.80%	0.26%	19.94%
Cyanidation areas	0%	72.26%	27.74%
Other types of land-uses	0.005%	0.04%	99.955%

Another source of error may arise from the extrapolation of the results obtained with Landsat 8 to Landsat 7 and 5 as a consequence of the minor differences in the shape of the filters in certain bands (see Figure S2 in Supporting Information S1 for more details). A test of the consequence of extrapolating the result from one sensor to another may be achieved by examining the results over the same period of time using two different sensors (when two sensors were active at the same time). The Landsat data collection were examined in search for such a possibility (cloud-free images only) and only one possible case suitable for this comparison was found. The Landsat TM 5 image from January 1999 (Figure 14a) was compared to the Landsat ETM 7+ image from July 1999 (Figure 14b).

Both images highlight the extraction waste which appears in dark yellow in the Landsat TM 5 image and in light yellow in the Landsat ETM 7+ image. In both images, the PC3 and PC4 axes are reversed in the RGB combination because of the similarity between PC3 in the TM5 image and PC4 in the ETM7+ image. This similarity is due to the fact that hydroxyl-bearing minerals are always highlighted in either PC3 or PC4 of the hydroxyl-bearing minerals FPCS (Loughlin, 1991). This validation and test are considered to be sufficient to justify the application of the FPCS for hydroxyl-bearing minerals to the entire Landsat time series. The results are presented in the next section.

5. Application to the Time Series and Discussion

The FPCS for hydroxyl-bearing minerals is applied to the selection of suitable Landsat images over Koma Bangou. Figure 15 shows the extent of waste in the Koma Bangou gold panning site for illustration of the method applied to Landsat images in the past, with four different periods: July 1988 (Figure 15a), June 2001 (Figure 15b), November 2010 (Figure 15c) and April 2020 (Figure 15d). The cyanidation waste does not appear on images acquired in 1988 and 2001, because cyanidation treatment took place at a later time (2009). For these images, the extraction areas are mapped and appear in green (Figures 15a and 15b). The two images from 2010 (Figure 15c) and 2020 (Figure 15d) are characterized by the presence and accelerated extension of both extraction and cyanidation waste areas. The cyanidation treatment, introduced in 2009, is noticed in 2010 image (Figure 15c), with three small yellow cyanidation areas, whereas extraction areas

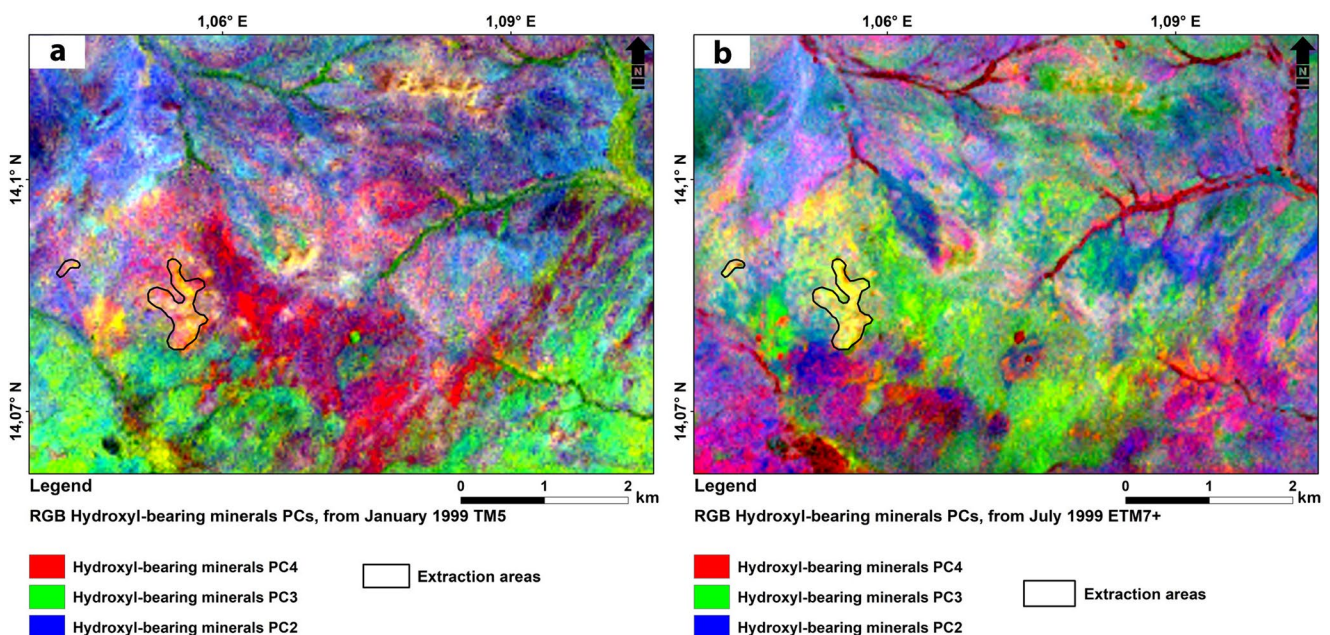


Figure 14. Comparison of a Landsat TM 5 image from January 1999 (a) with a Landsat Enhanced Thematic Mapper 7+ image from July 1999 (b).

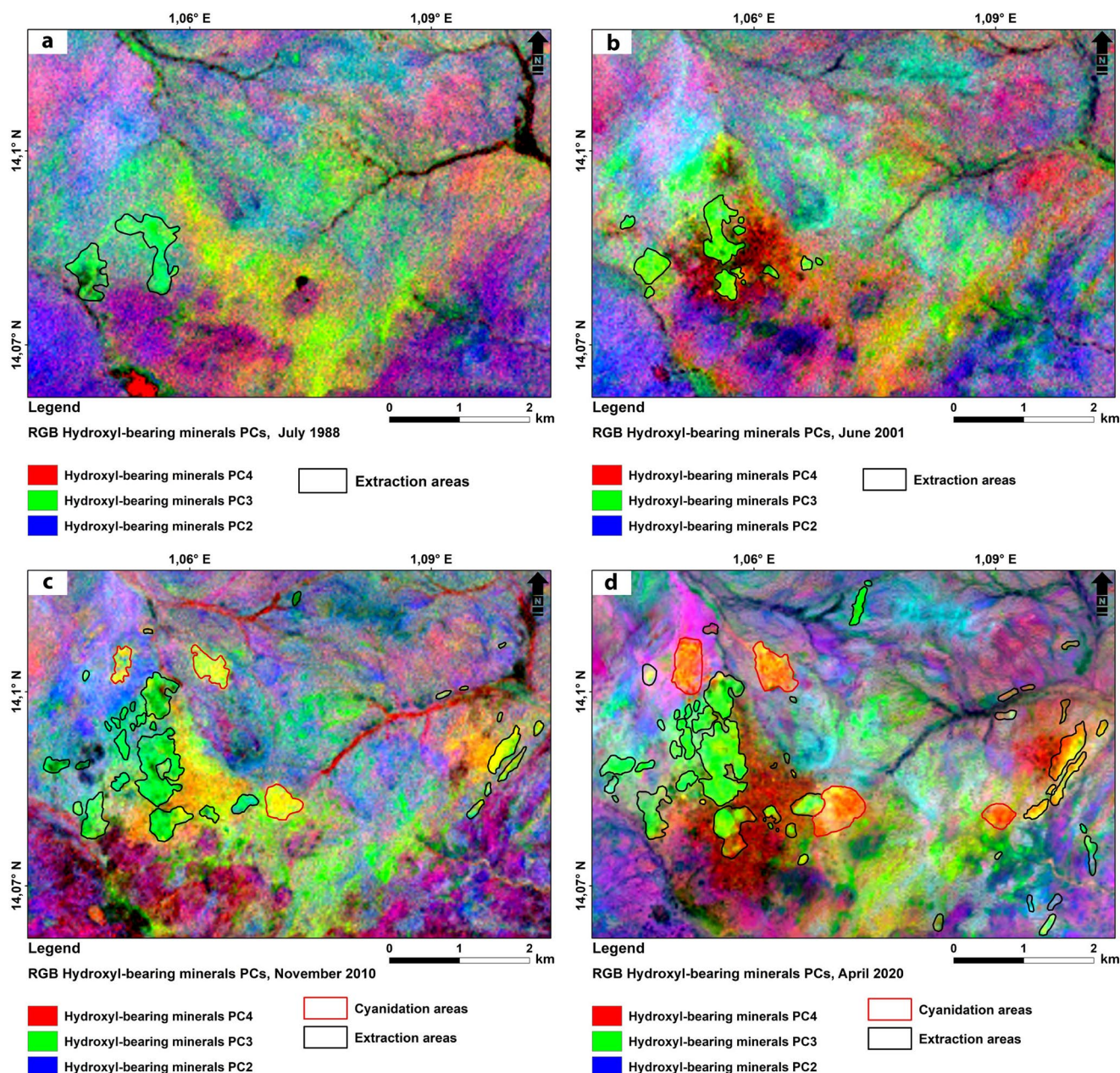


Figure 15. Extent of the Koma Bangou gold panning waste areas: (a) July 1988; (b) June 2001; (c) November 2010; (d) April 2020. Extraction areas appear in greenish hues, cyanidation areas in yellowish hues (for 2010 and 2020 images only).

appear in green to greenish-yellow hues. The 2020 image (Figure 15d) shows green and reddish-yellow extraction areas and four reddish-yellow cyanidation areas.

The various Landsat images are used to map the evolution of artisanal gold mining in the Koma Bangou area. The results of the gold panning waste areas with gold price by year (Bourse de Luxembourg, 2021) between 1984 and 2020 (Figure 16; Table S2 in Supporting Information S2) highlight the progressive evolution of the gold mining areas and the influence of the gold price. The first period of gold panning from 1984 to 1989 was characterized by a small change of waste production from 9.43 ha in 1984 to 17.07 ha (1989). This is probably due to the small number of gold miners at the start of the gold panning activities at the Koma Bangou site, the lack of enthusiasm for gold panning and the lower price of gold during this period. Most people went into gold panning to cope with the famine. The period of closure of the Koma Bangou gold

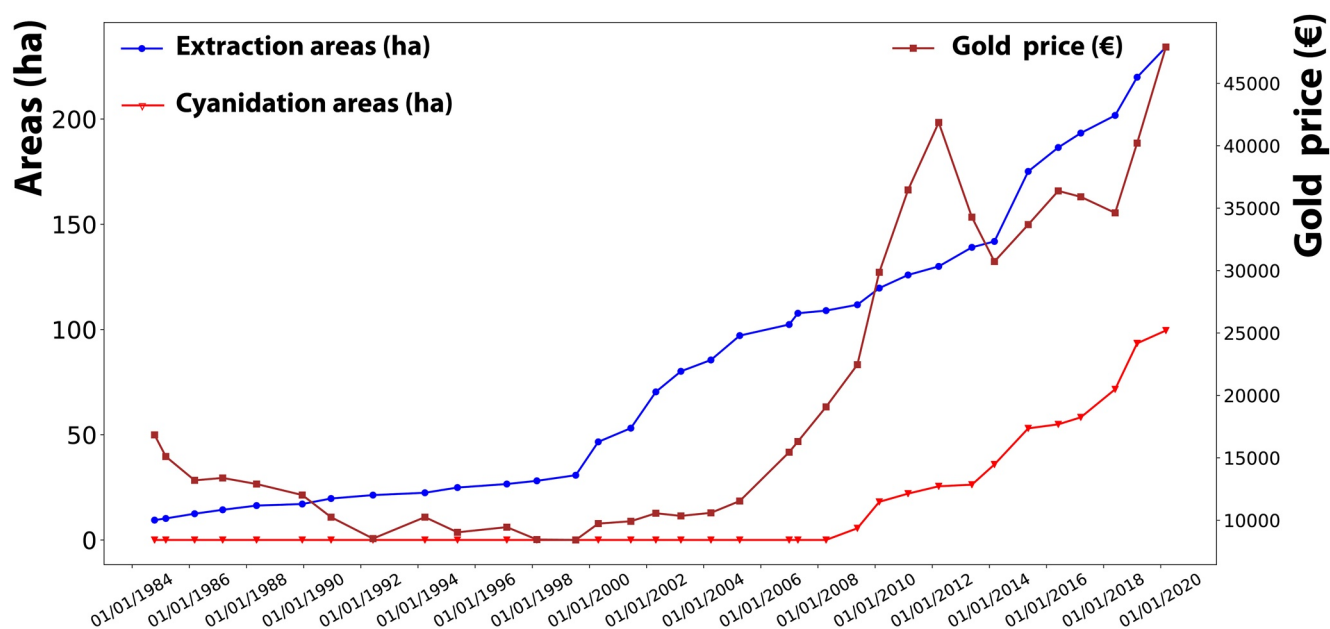


Figure 16. The Koma Bangou gold panning site waste surface evolution with the price of gold from 1984 to 2020.

panning site (1989–1999) was marked by a phase of clandestine gold panning. The extraction waste areas increased from 17.07 ha in 1989 to 28.10 ha in 1998. After the Koma Bangou prospect gold reserves estimated between 1998 and 1999 by industrial companies (gold reserves non exploitable at that time), the site was reclassified as gold panning site in the year 1999. From 1999 to the present day, with the increase of gold panners number according to the gold rushes on the site, the extraction waste increased from 30.76 ha (1999) to 234.20 ha in March 2020. The craze for gold panning since the year 2000 is due to the rise of gold price since that year (Figure 16). This led to a rapid expansion of extraction waste areas from 2000 to present.

With the introduction of tailings cyanidation in 2009, in Niger, by gold panners who came from Burkina Faso, the cyanidation waste was gaining ground at Koma Bangou since then. The cyanidation waste surface increased, from 5.56 ha (2009) to 99.53 ha in March 2020 (Figure 16). The rise of the gold price led gold miners to value the waste from gravimetric treatment by using chemical methods derived from the gold mining industry. The very satisfactory results of the cyanide treatment made that large quantities of tailings were stored at the Koma Bangou site from 2009 to 2020. Cyanidation areas were quickly multiplied on the site and large piles of polluted mine waste were formed (Ousseini Zakaria et al., 2019; Tankari Dan-Badjo et al., 2014, 2019).

6. Conclusion

The processing of Landsat images from 1984 to 2020 of the Koma Bangou area has made it possible to map and monitor the evolution of gold mining waste in this area. Of all the processing techniques designed to highlight mining areas and applied to the Landsat images, the FPCS technique applied to hydroxyl-bearing minerals is the most effective in highlighting and mapping the waste areas. This processing technique also enables the identification of the expansion of illegal gold mining during 1989–1999 period. At the end of this treatment, it appears that gold extraction waste rich in hydroxyl-bearing minerals, easily identified by FPCS and BR for hydroxyl-bearing minerals, does not have the same spectral signatures as the waste from the cyanidation areas. Cyanidation waste, rich in fine silica particles and various metals, such as zinc and mercury used in chemical processing, has particular spectral signatures that are not consistent with conventional BRs.

Therefore, it is necessary to carry out field spectroradiometry and field geochemistry to characterize the spectra and geochemistry of this cyanidation waste in terms of the content of heavy metals such as zinc and mercury used in the treatment and which end up as pollutants in soils and water resources.

The Landsat images perform well for the identification and mapping of gold mining waste. These images allow the evolution of the gold panning activities to be monitored, especially in the Sahel, with low vegetation cover. The fact that these images are publicly available and easily accessible is also an important asset for this study, and for future studies in Niger, and more regionally in west Africa.

Finally, future works might focus on comparing the performance of Landsat 8 and Sentinel 2 images, over the same periods for mapping and monitoring recent sites. The two sensors have similar but not exactly identical spectral bands. The determination of the most efficient sensor may be useful for the design of future imaging systems optimized for the monitoring of mining environments, among other possible applications.

Conflict of Interest

The authors declare no conflicts of interest relevant to this study.

Data Availability Statement

This manuscript uses publicly available Landsat 4, 5, 7, and 8 data, downloaded from the USGS server <http://earthexplorer.usgs.gov>.

Acknowledgments

This work was made possible through support provided by the French National Research Institute for Sustainable Development (IRD) and the French Development Agency (AFD). The authors thank to the Geochemical Society, the International Mixed Laboratory for Responsible Mining Activity in West Africa (LMI-MINERWA) and the ACE-Partners for Sustainable mining activities for their financial support; D. Baratoux and L. Baratoux acknowledge support from IRD and University Félix Houphouët-Boigny (UFHB) during their stay in Côte d'Ivoire (started in January 2021). The authors thank two anonymous reviewers for their valuable comments, which helped us to improve the manuscript.

References

- Abaidoo, C. A., Osei Jnr, E. M., Arko-Adjei, A., & Prah, B. E. K. (2019). Monitoring the extent of reclamation of small scale mining areas using artificial neural networks. *Heliyon*, 5, 21. <https://doi.org/10.1016/j.heliyon.2019.e01445>
- Abdelsalam, M. G., Stern, R. J., & Berhane, W. G. (2000). Mapping gossans in arid regions with Landsat TM and SIR-C images: The Beddaho alteration zone in northern Eritrea. *Journal of African Earth Sciences*, 30, 903–916. [https://doi.org/10.1016/S0899-5362\(00\)00059-2](https://doi.org/10.1016/S0899-5362(00)00059-2)
- Abhary, A., & Hassani, H. (2016). Mapping hydrothermal mineral deposits using PCA and BR methods in BAFT 1:100000 geological sheet, Iran. *International Journal of Advanced Engineering, Management and Science*, 2(9), 1433–1438.
- Abrams, M. J., Brown, D., Lepley, L., & Sadowski, R. (1983). Remote sensing for porphyry copper deposits in southern Arizona. *Economic Geology*, 78, 591–604. <https://doi.org/10.2113/gsecongeo.78.4.591>
- Adon Simon, A., Gnamien Jean-Claude, K. K., & Moussa, S. (2016). Impacts sociaux et environnementaux de L'orpaillage sur les populations de la region du Bounkani (Cote D'ivoire). *European Scientific Journal*, 12, 288. <https://doi.org/10.19044/esj.2016.v12n26p288>
- Alibert, P., Beis, P., Bermond, A., Bohard, B., Camizuli, E., Delivet, G., et al. (2011). Le projet « Identification et impact des sites miniers abandonnés sur les écosystèmes aquatiques et terrestres actuels. *Revue Scientifique Bourgogne-Nature*, 13–2011, 37–41. Retrieved from <https://halshs.archives-ouvertes.fr/halshs-00659178>
- Aliyu, O., & Aliyu, K. (2020). Utilizing landsat-8 sensor operational land image data for hydrothermal alteration mapping within Anka Schist Belt, northwestern Nigeria. *Zb Depart geogr, turizam i hotel*, 127–149. <https://doi.org/10.5937/ZbDgth2002127A>
- Alshaebi, F. Y., Yaacob, W. Z. W., Samsudin, A. R., & Alsabahi, E. (2009). Risk assessment at abandoned Tin Mine in Sungai Lembing, Pahang, Malaysia (Vol. 14). Retrieved from <https://citeseerx.ist.psu.edu/viewdoc/download?doi=10.1.1.615.8974&rep=rep1&type=pdf>
- Amadou, M. D., & Bouzou, M. I. (2016). Evaluation et cartographie de la dégradation des terres des sites aurifères du Liptako nigérien par l'analyse multicritère couplée au SIG. *Revue Sciences de l'Environnement. Université de Lomé (Togo)*, 13.
- Association Vie et Développement. (2018). *Rapport sur l'inventaire des sources de rejet du mercure au Niger (Rapport Final)*. AVD-Kowa Murna, Niamey 54. Retrieved from https://ipen.org/sites/default/files/documents/rapport_final_csr_mercure_niger_avd_1-1.pdf
- Barenblitt, A., Payton, A., Lagomasino, D., Fatoyinbo, L., Asare, K., Aidoo, K., et al. (2021). The large footprint of small-scale artisanal gold mining in Ghana. *The Science of the Total Environment*, 781, 146644. <https://doi.org/10.1016/j.scitotenv.2021.146644>
- Berman, M. (1985). *The statistical properties of three noise removal procedures for multi channel remotely sensed data*. (Consulting Report No. NSW/85/31/MB9). CSIRO Division of Mathematics and Statistics 37.
- Boardman, J. W., Kruse, F. A., & Green, R. O. (1995). *Mapping target signatures via partial unmixing of aviris data 4*. Retrieved from https://aviris.jpl.nasa.gov/proceedings/workshops/95_docs/7.PDF
- Boateng, D. Y. A., Morufdeen, A. A., Jnr, E. M. O., & Ntori, C. (2018). Hydrothermal alteration mapping, using the crosta technique: Case study of the Kibi goldfields osino concession, Ghana 8. Retrieved from <https://www.researchgate.net/publication/330244348>
- Callil, C. T., & Junk, W. J. (2010). *Gold-mining near Poconé: Environmental, social and economic impact* (pp. 693–715). Pensoft Publishers. Retrieved from https://www.researchgate.net/publication/260889117_Gold_mining_near_Pocone_Environmental_social_and_economic_impact
- Carranza, E. J. M., & Hale, M. (2002). Mineral imaging with Landsat thematic mapper data for hydrothermal alteration mapping in heavily vegetated terrane. *International Journal of Remote Sensing*, 23, 4827–4852. <https://doi.org/10.1080/01431160110115014>
- Chica-Olmo, M., Abarca, F., & Rigol, J. P. (2002). Development of a decision support system based on remote sensing and GIS techniques for gold-rich area identification in SE Spain. *International Journal of Remote Sensing*, 23, 4801–4814. <https://doi.org/10.1080/014311601101104656>
- Ciampalini, A., Garfagnoli, F., Antonielli, B., Moretti, S., & Righini, G. (2013). Remote sensing techniques using Landsat ETM+ applied to the detection of iron ore deposits in Western Africa. *Arabian Journal of Geoscience*, 6, 4529–4546. <https://doi.org/10.1007/s12517-012-0725-0>
- Clark, R. N. (1999). *USGS Spectroscopy Lab: Spectroscopy of Rocks and Minerals, and Principles of Spectroscopy* (Vol. 293). USGS. Retrieved from <http://speclab.cr.usgs.gov>

- Crósta, A. P., De Souza Filho, C. R., Azevedo, F., & Brodie, C. (2003). Targeting key alteration minerals in epithermal deposits in Patagonia, Argentina, using ASTER imagery and principal component analysis. *International Journal of Remote Sensing*, 24, 4233–4240. <https://doi.org/10.1080/0143116031000152291>
- Crósta, A. P., & Moore, J. M. (1989). Enhancement of Landsat thematic mapper imagery for residual soil mapping in SW Minas Gerais State, Brazil: A prospecting case history in Greenstone belt terrain. In *Proceedings of the 7th (ERIM) Thematic Conference: Remote Sensing for Exploration Geology* (pp. 1173–1187). Retrieved from <https://www.researchgate.net/publication/284966233>
- Dabiri, Z., & Lang, S. (2018). Comparison of independent component analysis, principal component analysis, and minimum noise fraction transformation for tree species classification using APEX hyperspectral imagery. *ISPRS International Journal of Geo-Information*, 7, 488. <https://doi.org/10.3390/ijgi7120488>
- Dadon, A., Ben-dor, E., & Karnieli, A. (2010). Use of derivative calculations and minimum noise fraction transform for detecting and correcting the spectral curvature effect (smile) in hyperion images. *IEEE Transactions on Geoscience and Remote Sensing*, 48, 2603–2612. <https://doi.org/10.1109/tgrs.2010.2040391>
- de Luxembourg, B. (2021). *Métaux précieux en Bourse de Luxembourg 1981–2020*. [WWW Document]. Bourse de Luxembourg Retrieved from https://statistiques.public.lu/stat/TableViewer/tableViewHTML.aspx?ReportId=13546&IF_Language=fra&MainTheme=4&FldrName=8&RFPPath=7
- Dupuis, D., Pons, J., & Prost, E. A. (1991). Mise en place de plutons et caractérisation de la déformation birimienne au Niger occidental. *Tectonics. Compte Rendu Académie des Sciences Paris*, 312, 769–776.
- Forkuor, G., Ullmann, T., & Griesbeck, M. (2020). Mapping and monitoring small-scale mining activities in Ghana using Sentinel-1 time series (2015–2019). *Remote Sensing*, 12, 911. <https://doi.org/10.3390/rs12060911>
- Frassy, F., Dalla Via, G., Maiani, P., Marchesi, A., Nodari, F. R., & Gianinetti, M. (2013). *Minimum noise fraction transform for improving the classification of airborne hyperspectral data: Two case studies* (pp. 1–4). IEEE. <https://doi.org/10.1109/WHISPERS.2013.8080626>
- Frutuoso, R. (2015). Mapping hydrothermal gold mineralization using Landsat 8 data. In *A Case of Study in Chaves License* (Vol. 85). Memoire de Master de géologie, Université de Porto.
- Gabr, S., Ghulam, A., & Kusky, T. (2010). Detecting areas of high-potential gold mineralization using ASTER data. *Ore Geology Reviews*, 38, 59–69. <https://doi.org/10.1016/j.oregeorev.2010.05.007>
- Garba Hamidou, I. (2019). *Orpaillages au Niger: Entre prospérité des hommes et dégradation de l'environnement*. [WWW Document]. Retrieved from <https://www.niameysoir.com/orpaillages-au-niger-entre-prosperte-des-hommes-et-degradation-de-lenvironnement/>
- Gond, V., Petit, M., & collab (2004). *Potential de la télédétection pour la surveillance de l'orpaillage: Rapport final convention de consultation institutionnelle IRD-Conseil Régional 22*. Retrieved from https://horizon.documentation.ird.fr/exl-doc/pleins_textes/di-vers19-12/010036613.pdf
- Grandin, G., & Traoré, D. (1991). Projet de recherche pluridisciplinaire sur l'orpaillage: Compte-rendu de la réunion du 05/11/1991 au centre ORSTOM de Ouagadougou. *Fonds Documentaire ORSTOM 23*. https://horizon.documentation.ird.fr/exl-doc/pleins_textes/pleins_textes_6/b_fdi_45-46/010009480.pdf
- Green, A. A., Berman, M., Switzer, P., & Craig, M. D. (1988). A transformation for ordering multispectral data in terms of image quality with implications for noise removal. *IEEE Transactions on Geoscience and Remote Sensing*, 26, 65–74. <https://doi.org/10.1109/36.3001>
- Grégoire, E., & Gagnol, L. (2017). Ruées vers l'or au Sahara : L'orpaillage dans le désert du Ténéré et le massif de l'Air (Niger). *EchoGéo*, 22. <https://doi.org/10.4000/echogeo.14933>
- Han, T., & Nelson, J. (2014). Mapping hydrothermally altered rocks with Landsat 8 imagery: A case study in the KSM and Snoweld zones, northwestern British Columbia. *British Columbia Geological Survey 10*. Retrieved from http://cmscontent.nrs.gov.bc.ca/geoscience/publicationcatalogue/Paper/BCGS_P2015-01-06_Han.pdf
- Hao, L., Zhang, Z., & Yang, X. (2019). Mine tailing extraction indexes and model using remote-sensing images in southeast Hubei Province. *Environmental Earth Sciences*, 78, 493. <https://doi.org/10.1007/s12665-019-8439-1>
- Harris, J., Rogge, D., Hitchcock, R., Ijewliw, O., & Wright, D. (2011). Mapping lithology in Canada's Arctic: Application of hyperspectral data using the minimum noise fraction transformation and matched filtering. *Canadian Journal of Earth Sciences*, 42, 2173–2193. <https://doi.org/10.1139/e05-064>
- Hentschel, T., Hruschka, F., & Priester, M. (2002). *Artisanal and small-scale mining* (pp. 315–334). Retrieved from <https://www.researchgate.net/publication/315412933>
- Hilson, G. (2002). The environmental impact of small-scale gold mining in Ghana: Identifying problems and possible solutions. *The Geographical Journal*, 168, 57–72. <https://doi.org/10.1111/1475-4959.00038>
- Hilson, G. (2009). Small-scale mining, poverty and economic development in sub-Saharan Africa: An overview. *Resources Policy, Small-Scale Mining, Poverty and Development in Sub-Saharan Africa*, 34, 1–5. <https://doi.org/10.1016/j.resourpol.2008.12.001>
- Hilson, G. (2016). Farming, small-scale mining and rural livelihoods in Sub-Saharan Africa: A critical overview. *The Extractive Industries and Society*, 3, 547–563. <https://doi.org/10.1016/j.exis.2016.02.003>
- Hilson, G. (2020). The Africa mining vision: A manifesto for more inclusive extractive industry-led development? *Canadian Journal of Development Studies/Revue Canadienne d'Études du Développement*, 41, 417–431. <https://doi.org/10.1080/02255189.2020.1821352>
- Hilson, G., Goumandakoye, H., & Diallo, P. (2019). Formalizing artisanal mining 'spaces' in rural sub-Saharan Africa: The case of Niger. *Land Use Policy*, 80, 259–268. <https://doi.org/10.1016/j.landusepol.2018.09.023>
- Hung, T. L. (2013). Method of monitoring minerals using remote sensing data based on spectral index. *Vestnik OreIGA*, 6(45), 5. Retrieved from <https://cyberleninka.ru/article/n/method-of-monitoring-minerals-using-remote-sensing-data-based-on-spectral-index/pdf>
- Imbroane, M. A., Melenti, C., & Gorgan, D. (2007). *Mineral explorations by Landsat image Ratios SYNASC 2007*. IEEE, Timisoara Romania. (pp.335–340). <https://doi.org/10.1109/SYNASC.2007.52>
- Jennings, N. (1999). *Social and labour issues in small-scale mines*. Report, International Labour Office, Geneva 99. Retrieved from https://www.ilo.org/wcmsp5/groups/public/---ed_dialogue/---sector/documents/meetingdocument/wcms_714371.pdf
- Keita, A. (2017). *Orpaillage et accès aux ressources naturelles et foncières au Mali* (Vol. 29). CIRDIS. Retrieved from https://www.ieim.uqam.ca/IMG/pdf/cahier_cirdis_-_no2017_-_01.pdf
- Keita, S. (2001). *Etude sur les mines artisanales et les exploitations minières à petite échelle au mali*. Mining, minerals and sustainable development (Vol. 54). Retrieved from <https://pubs.iied.org/sites/default/files/pdfs/migrate/G00727.pdf?>
- Khalifa, I. H., & Arnous, M. O. (2012). Assessment of hazardous mine waste transport in west central Sinai, using remote sensing and GIS approaches: A case study of Um Bogma area, Egypt. *Arabian Journal of Geosciences*, 5, 407–420. <https://doi.org/10.1007/s12517-010-0196-0>
- Khidir, S. O. E., & Babikir, I. A. A. (2013). Digital image processing and geospatial analysis of landsat 7 ETM+ for mineral exploration, Abidiya area, North Sudan. *International Journal of Geomatics and Geosciences*, 3, Retrieved from <http://www.indianjournals.com/ijor.Asp?target=ijor:ijggs&volume=3&issue=3&article=021>

- Kokaly, R. F., Clark, R. N., Swayze, G. A., Livo, K. E., Hoefen, T. M., Pearson, N. C., et al. (2017). USGS Spectral Library Version 7 (Data Series 1035), Data Series. *U.S. Geological Survey*, 61. <https://doi.org/10.3133/ds1035>
- Kuijjo, C., Liang, L., & Ravat, D. (2018). Mapping hydrothermal alteration zones in the Didinga hills, South Sudan. *International Journal of Remote Sensing & Geoscience (IJRSG)*, 7(2). Retrieved from http://www.ijrsg.com/Files/ef11216e-a945-471a-ad9a-c30fd21c0c9c_IJRSG_35_01.pdf
- Kumar, C., Shetty, A., Raval, S., Sharma, R., & Ray, P. K. C. (2015). Lithological discrimination and mapping using ASTER SWIR Data in the Udaipur area of Rajasthan, India. *Procedia Earth and Planetary Science*, 11, 180–188. <https://doi.org/10.1016/j.proeps.2015.06.022>
- Loughlin, W. P. (1991). Principal component analysis for alteration mapping. *Photogrammetric Engineering and Remote Sensing*, 57, 1163–1169. Retrieved from https://www.asprs.org/wp-content/uploads/pers/1991journal/sep/1991_sep_1163-1169.pdf
- Machens, E. (1967). Notice explicative sur la carte géologique du Niger Occidental, Carte géol. 1/200 000ème. *Mines Géology*.
- Machens, E. (1973). *Contribution à l'étude des formations du socle cristallin et de la couverture sédimentaire de l'Ouest de la République du Niger* (Vol. 82, pp. 157). Mémoires du B.R.G.M No.
- Mallo, S. J. (2012). Mitigating the activities of artisanal and small-scale miners in Africa: Challenges for engineering and technological institutions. *International Journal of Modern Engineering Research (IJMER)*, 2(6), 4714–4725. Retrieved from http://www.ijmer.com/papers/Vol2_Issue6/FC2647144725.pdf
- Marcangeli, Y. (2003). *Cartographie des zones dégradées par l'exploitation minière*: Mémoire DESS Ingénierie de l'Ecologie, Université de Corse Pascal Paoli.
- Martin, A., & Hélène, H. de B. (2017). *The West Africa El Dorado: Mapping the Illicit Trade of Gold in Côte d'Ivoire, Mali and Burkina Faso*. *Partnership Africa Canada* (Vol. 28). Retrieved from https://media.africaportal.org/documents/PAC_El_Dorado_Jan_2016_EN.pdf
- Masoumi, F., Eslamkish, T., Honarmand, M., & Abkar, A. A. (2017). A comparative study of Landsat-7 and Landsat-8 data using image processing methods for hydrothermal alteration mapping. *Resource Geology*, 67, 72–88. <https://doi.org/10.1111/rge.12117>
- Mensah, E., Wapaburda, S., & Hammond, F. (2017). A hybrid image classification approach to monitoring LULC changes in the mining district of Prestea-Huni Valley, Ghana. *Journal of Environment and Earth Science*, 7(3), 10. Retrieved from <https://core.ac.uk/download/pdf/234664848.pdf>
- Mia, B., & Fujimitsu, Y. (2012). Mapping hydrothermal altered mineral deposits using Landsat 7 ETM+ image in and around Kuju volcano, Kyushu, Japan. *Journal of Earth System Science*, 121, 1049–1057. <https://doi.org/10.1007/s12040-012-0211-9>
- Milési, J.-P., Feybesse, J.-L., Pinna, P., Deschamps, Y., Kampunzu, H., Muhonogo, S., et al. (2004). Géologie et principaux gisements de l'Afrique. *échelle*. 1/10,000,000.
- Ministère des Mines et de l'énergie. (2006). *Décret d'application de la loi minière*. Décret n 2006-265/PRN/MM/E du 18 août 2006 23. Retrieved from <http://extwprlegs1.fao.org/docs/pdf/Ner190573.pdf>
- Mkpuma, R. O., Okeke, O. C., & Abraham, E. M. (2015). Environmental problems of surface and underground mining: A review. *International Journal of Engineering Science*, 4(12), 12–20. <http://theijes.com/papers/v4-i12/Version-2/C041202012020.pdf>
- Mobbs, P. M. (1997). *The mineral industry of Niger*, 3. <https://s3-us-west-2.amazonaws.com/prd-wret/assets/palladium/production/mineral-pubs/country/1997/9247097.pdf>
- Mohammady, M., Moradi, H. R., Zeinivand, H., Temme, A. J. A. M., Pourghasemi, H. R., & Alizadeh, H. (2014). Validating gap-filling of Landsat ETM+ satellite images in the Golestan Province, Iran. *Arabian Journal of Geosciences*, 7, 3633–3638. <https://doi.org/10.1007/s12517-013-0967-5>
- Moradi, R., & Boomeri, M. (2017). Remote sensing detection of altered zones associated with Cu-Mo mineralization in North of Zahedan, SE Iran using Landsat-8 data. *Bulletin of the Earth Sciences Application and Research Centre of Hacettepe University*, 38(3), 275–294. Retrieved from http://www.yerbilimleri.hacettepe.edu.tr/383/383_4.pdf
- Mudd, G. M. (2007). Global trends in gold mining: Towards quantifying environmental and resource sustainability. *Resources Policy*, 32, 42–56. <https://doi.org/10.1016/j.resourpol.2007.05.002>
- Mwaniki, M. W., Moeller, M. S., & Schellmann, G. (2015). A comparison of Landsat 8 (OLI) and Landsat 7 (ETM+) in mapping geology and visualising lineaments: A case study of central region Kenya. *International Archives of Photogrammetry, Remote Sensing and Spatial Information Sciences*, XL-7/W3, 897–903. <https://doi.org/10.5194/isprsarchives-XL-7-W3-897-2015>
- NASA. (2014). *Spectral response of the operational land imager in-band, band-average relative spectral response* [WWW Document]. Landsat Science. Retrieved from <https://landsat.gsfc.nasa.gov/landsat-8/spectral-response-operational-land-imager-band-band-average-relative-spectral-response>
- NASA. (2017). *Spectral characterization* [WWW Document]. Landsat science. Retrieved from <https://landsat.gsfc.nasa.gov/about/spectral-characterization>
- Ngom, N. M., Mbaye, M., Baratoux, D., Baratoux, L., Catry, T., Dessay, N., et al. (2020). Mapping artisanal and small-scale gold mining in Senegal using Sentinel 2 Data. *GeoHealth*, 4, e2020GH000310. <https://doi.org/10.1029/2020GH000310>
- Nodem, F. R., Sangodoyin, A. Y., Kegne, I. M., & Ntep, F. (2019). Spatial assessment of impacts of artisanal and small-scale mining on land cover and environment, Batouri, Eastern Cameroun. *African Journal of Land Policy and Geospatial Sciences*, 2(3), 85–96. ISSN2657-2664. <https://revues.imist.ma/index.php/AJLP-GS/article/view/14372/9868>
- Omara, T., Karungi, S., Ssebulime, S., Kiplagat, K. M., Bongomin, O., Ogwang, R., & Akaganyira, S. (2019). Artisanal and small-scale gold mining in Syanyonja, Busia Gold District, South Eastern Uganda: Impacts on the mining population and the environment (preprint). *Earth Sciences*. <https://doi.org/10.20944/preprints201910.0298.v1>
- Organisation de Coopération et de Développement Économiques. (2018). *L'or à la croisée des chemins : Étude d'évaluation des chaînes d'approvisionnement en or produit au Burkina Faso, au Mali et au Niger* (Vol. 70). Guide OCDE. Retrieved from <http://mneguidelines.oecd.org/Evaluation-des-chaines-appvisionnement-en-or-produit-au-Burkina-Faso-Mali-Niger.pdf>
- Organisation Internationale du Travail. (2009). Sécurité et optimisation des techniques d'exploitation et de traitement sur les sites d'orpaillage de Komabangou et M'Banga. *Rapport Final No. Projets BIT/IPEC Mines (Afrique de l'Ouest) RAF/05/54/USA 51*.
- Osinowo, O. O., Gomy, A., & Isseini, M. (2021). Mapping hydrothermal alteration mineral deposits from Landsat 8 satellite data in Pala, Mayo Kebbi Region, Southwestern Chad. *Scientific African*, 11, e00687. <https://doi.org/10.1016/j.sciaf.2020.e00687>
- Ourhizif, Z., Algouti, A., Algouti, A., & Hadach, F. (2019). Lithological mapping using Landsat 8 oli and aster multispectral data in Imi-ni-Ounilla district south high atlas of Marrakech. *International Archives of Photogrammetry, Remote Sensing and Spatial Information Sciences*, XLII-2/W13, 1255–1262. <https://doi.org/10.5194/isprs-archives-XLII-2-W13-1255-2019>
- Ousseini Zakaria, I., Dan-Badjo, A. T., Elhadji, I., Gado, F. A., Ambouta, K. J. M., & Guero, Y. (2018). Impact of gold mining on vegetation at Komabangou area. *International Journal of Current Research*, 10, 74554–74558. <https://doi.org/10.24941/ijcr.32761.10.2018>

- Ousseini Zakaria, I., Dan-Badjo, A. T., Guero, Y., Idi, F. M. M., Feidt, C., Sterckeman, T., & Echevarria, G. (2019). Distribution spatiale des éléments traces métalliques dans les sols de la zone aurifère de Komabangou au Niger. *International Journal of Biological and Chemical Sciences*, 13, 557–573. <https://doi.org/10.4314/ijbcs.v13i1.43>
- Owusu, E. E., & Dwomoh, D. G. (2012). The impact of illegal mining on the Ghanaian youth: Evidence from Kwaebibirem District in Ghana. *Research on Humanities and Social Sciences*, 2, 86–93. Retrieved from <https://core.ac.uk/download/pdf/234673195.pdf>
- Owusu, O., Bansah, K. J., & Mensah, A. K. (2019). “Small in size, but big in impact”: Socio-environmental reforms for sustainable artisanal and small-scale mining. *Journal of Sustainable Mining*, 18, 38–44. <https://doi.org/10.1016/j.jsm.2019.02.001>
- Paull, D., Banks, G., Ballard, C., & Gillieson, D. (2006). Monitoring the environmental impact of mining in remote locations through remotely sensed data. *Geocarto International*, 21, 33–42. <https://doi.org/10.1080/10106040608542372>
- Pellerin, M. (2017). *Beyond the “wild west”. The gold rush in northern Niger*. Retrieved from <http://www.smallarmssurvey.org/fileadmin/docs/T-Briefing-Papers/SAS-SANA-BP-Niger-Gold.pdf>
- Pétot, J. (1995). *Reorganisation et modernisation de la petite industrie de l’orpaillage au liptako Niger* (pp. 85). Projet SI/NER./93/803/11-51.
- Plumlee, G. S. (1997). The environmental geology of mineral deposits. *U.S. Geological Survey*, 46. <https://doi.org/10.5382/Rev.06.03>
- Poormirzaee, R., & Oskouei, M. M. (2010). Use of spectral analysis for detection of alterations in ETM data, Yazd, Iran. *Applied Geomatics*, 2, 147–154. <https://doi.org/10.1007/s12518-010-0027-8>
- Poulin, R., Kima, A., & Savard, R. (1987). *Campagne de prospection 1986-87 à Koma Bangou, Niger. Tome 1* (No. 227). Ministère des Mines et de l’énergie.
- Pour, A. B., Park, T.-Y. S., Park, Y., Hong, J. K., Muslim, A. M., Läufer, A., et al. (2019). Landsat-8, advanced spaceborne thermal emission and reaction radiometer, and WorldView-3 multispectral satellite imagery for prospecting copper-gold mineralization in the northeastern ingeleld mobile belt (IMB), Northwest Greenland. *Remote Sensing*, 11, 243039. <https://doi.org/10.3390/rs11202430>
- Pournamdari, M., Hashim, M., & Pour, A. B. (2014). Application of ASTER and Landsat TM data for geological mapping of Esfandagheh ophiolite complex, Southern Iran. *Resource Geology*, 64, 233–246. <https://doi.org/10.1111/rge.12038>
- Ramadan, T. M., Abdelsalam, M. G., & Stem, R. J. (2001). Mapping gold-bearing massive sulfide deposits in the neoproterozoic Allaqi Suture, southeast Egypt with Landsat TM and SIR-C/X SAR images. *Photogrammetric Engineering & Remote Sensing*, 67(4), 491–497. Retrieved from https://www.asprs.org/wp-content/uploads/pers/2001journal/april/2001_apr_491-497.pdf
- Razack, A. A. (2002). Propositions pour l’optimisation de la mine artisanale au Niger Proposals for optimising artisanal mining in Niger. *Pangea infos, Société Géologique de France*, 37/38, 7–23. Retrieved from <https://hal-insu.archives-ouvertes.fr/insu-00947881>
- République du Niger. (2017). *Ordonnance 2017-03 du 30 juin 2017 portant modification de l’ordonnance n°93-16 du 02 mars 1993 portant loi minière* (Vol. 11). Retrieved from https://itieniger.ne/wp-content/uploads/2020/12/Ordonnance-2017-03-du-30-juin-2017_compressed.pdf
- Research Systems. (2003). *ENVI tutorials*. Edition Copyright © Research Systems, Inc. Retrieved from http://gers.uprm.edu/geol6225/pdfs/envy_tutorial.pdf
- Rigol-Sanchez, J. P., Chica-Olmo, M., & Abarca-Hernandez, F. (2003). Artificial neural networks as a tool for mineral potential mapping with GIS. *International Journal of Remote Sensing*, 24, 1151–1156. <https://doi.org/10.1080/0143116021000031791>
- Rockwell, B. W. (2013). *Automated Mapping of Mineral Groups and Green Vegetation from Landsat Thematic Mapper Imagery with an Example from the San Juan Mountains, Colorado* (Vol. 3252, pp. 31). Scientific Investigations Map. Retrieved from https://pubs.usgs.gov/sim/3252/downloads/pdfs/SIM3252_pamphlet.pdf
- Sabins, F. F. (1999). Remote sensing for mineral exploration. *Ore Geology Reviews*, 14, 157–183. [https://doi.org/10.1016/S0169-1368\(99\)00007-4](https://doi.org/10.1016/S0169-1368(99)00007-4)
- Scaramuzza, P., Micijevic, E., & Chander, G. (2004). *SLC gap-filled products phase one methodology*. Retrieved from <https://prd-wret.s3.us-west-2.amazonaws.com/assets/palladium/production/atoms/files/L7SLCgapFilledMethod.pdf>
- Schimmer, R. (2008). *A remote sensing and gis method for detecting land surface areas covered by copper mill tailings 13*. Retrieved from <https://www.asprs.org/a/publications/proceedings/pecora17/0030.pdf>
- Seyni, H. H., Ousmane, B., Soumana, I., & Yamba, B. (2014). Impacts des activités socio-économiques sur les ressources en eau du barrage de Tera au Niger. *Afrique Science*, 10(2), 149–172. Retrieved from <https://www.ajol.info/index.php/afsci/article/view/109660/99415>
- Shawky, M. M., El-Arafy, R. A., El Zalaky, M. A., & Elarif, T. (2019). Validating (MNF) transform to determine the least inherent dimensionality of ASTER image data of some uranium localities at Central Eastern Desert, Egypt. *Journal of African Earth Sciences*, 149, 441–450. <https://doi.org/10.1016/j.jafrearsci.2018.08.022>
- Sheriff, I., Gogra, A. B., & Koroma, B. M. (2018). Investigation into the Impacts of artisanal gold mining on the livelihood foundation of Baomahun community in southern Sierra Leone. *NR*, 09, 42–54. <https://doi.org/10.4236/nr.2018.92004>
- Soe, M., Kyaw, T. A., & Takashima, I. (2005). *Application of remote sensing techniques on iron oxide detection from ASTER and Landsat images of Tanintharyi coastal area* (Vol. 8). Retrieved from <https://core.ac.uk/download/pdf/144185813.pdf>
- Sonter, L. J., Moran, C. J., Barrett, D. J., & Soares-Filho, B. S. (2014). Processes of land use change in mining regions. *Journal of Cleaner Production*, 84, 494–501. <https://doi.org/10.1016/j.jclepro.2014.03.084>
- Soumaila, A. (2000). *Etude structurale, pétrographique et géochimique de la ceinture birimienne de Diagorou-Darbani Liptako, Niger Occidental (Afrique de l’ouest) (Thèse de Doctorat)* (Vol. 260). Université de Franche-comté. UFR des sciences et techniques.
- Storey, J., Scaramuzza, P., Schmidt, G., & Barsi, J. (2005). *Landsat 7 scan line corrector-off gap-filled product development 13*. Retrieved from https://www.asprs.org/a/publications/proceedings/pecora16/Storey_J.pdf
- Suresh, M., & Jain, D. K. (2013). Change detection and estimation of illegal mining using satellite images. In *Proceedings of 2nd international conference on innovations in electronics and communication engineering* (pp. 246–251). ICIECE-2013. Retrieved from https://www.researchgate.net/publication/260790784_Change_Detection_and_Estimation_of_Change_Analysis_using_Satellite_Images
- Swayze, G. A., Smith, K. S., Clark, R. N., Sutley, S. J., Pearson, R. M., Vance, J. S., et al. (2000). Using imaging spectroscopy to map acidic mine waste. *Environmental Science and Technology*, 34, 47–54. <https://doi.org/10.1021/es990046w>
- Tankari Dan-Badjo, A., Ibrahim, O. Z., Guéro, Y., Morel, J. L., Feidt, C., & Echevarria, G. (2019). Impacts of artisanal gold mining on soil, water and plant contamination by trace elements at Komabangou, Western Niger. *Journal of Geochemical Exploration*, 205, 106328. <https://doi.org/10.1016/j.gexplo.2019.06.010>
- Tankari Dan-Badjo, A., Tidjani, D. A., Idder, T., Guero, Y., Lamso, N. D., Matsallabi, A., et al. (2014). Diagnostic de la contamination des eaux par les éléments traces métalliques dans la zone aurifère de Komabangou – Tillabéri, Niger. *International Journal of Biological and Chemical Sciences*, 8, 2849–2857. <https://doi.org/10.4314/ijbcs.v8i6.41>
- Thiéblemont, D., Liégeois, J. P., ernandez-Alonso, M. O., Le Gall, A., Maury, B., Jalludin, R., et al. (2016). *Geological map of Africa*.

- Traore, M., Can, T., & Tekin, S. (2020). Discrimination of iron deposits using feature oriented principal component selection and band ratio methods: Eastern Taurus/TURKEY. *International Journal of Environment and Geoinformatics (IJEgeo)*, 7(2), 147–156. <https://doi.org/10.30897/ijegeo.673143>
- Van Der Meer, F. D., Dan Der Werff, H. M. A., Van Ruitenbeek, F. J. A., Hecker, C. A., Bakker, W. H., Noomen, M. F., et al. (2012). Multi- and hyperspectral geologic remote sensing: A review. *International Journal of Applied Earth Observation and Geoinformation*, 14, 112–128. <https://doi.org/10.1016/j.jag.2011.08.002>
- Werner, T. T., Bebbington, A., & Gregory, G. (2019). Assessing impacts of mining: Recent contributions from GIS and remote sensing. *The Extractive Industries and Society*, 6, 993–1012. <https://doi.org/10.1016/j.exis.2019.06.011>
- Werner, T. T., Mudd, G. M., Schipper, A. M., Huijbregts, M. A. J., Taneja, L., & Northey, S. A. (2020). Global-scale remote sensing of mine areas and analysis of factors explaining their extent. *Global Environmental Change*, 60, 102007. <https://doi.org/10.1016/j.gloenvcha.2019.102007>
- Woldai, T. (2001). *Application of remotely sensed data and GIS in assessing the impact of mining activities on the environment*. 17 (pp. 75–83). International Mining Congress and Exhibition of Turkey- IMCET2001. Retrieved from https://www.maden.org.tr/resimler/ekler/620005ac78d8257_ek.pdf
- Xu, X., Cai, H., Sun, D., Hu, L., & Banson, K. (2016). Impacts of mining and urbanization on the Qin-Ba mountainous environment, China. *Sustainability*, 8, 488. <https://doi.org/10.3390/su8050488>
- Yacouba, I. (2015). *Impacts environnemental et social des zones extractives: Cas de l'orpaillage dans la zone de Komabangou au Niger* (Vol. 46). Liaison Energie-Francophonie. Retrieved from <https://signal.sciencespo-lyon.fr/article/495139/Impacts-environnemental-et-social-des-zones-extractives-cas-de-l-orpaillage-dans-la-zone-de-Komabangou-au-Niger>
- Yonlihinza, I. A. (2017). *Mines - Niger : jusqu'où la ruée vers l'eldorado minéral?* [WWW Document] Retrieved from https://www.lepoint.fr/economie/mines-niger-jusqu-ou-la-ruée-vers-l-eldorado-mineral-16-05-2017-2127668_28.php
- Zhou, Q., Xian, G., & Shi, H. (2020). Gap fill of land surface temperature and reflectance products in landsat analysis ready data. *Remote Sensing*, 12, 1192. <https://doi.org/10.3390/rs12071192>

Reference From the Supporting Information

- Young, N. E., Anderson, R. S., Chignell, S. M., Vorster, A. G., Lawrence, R., & Evangelista, P. H. (2017). A survival guide to Landsat preprocessing. *Ecology*, 98, 920–932. <https://doi.org/10.1002/ecy.1730>